Metallic-like Stoichiometric Copper Sulfide Nanocrystals: Phase- and Shape-Selective Synthesis, Near-Infrared Surface Plasmon Resonance Properties, and Their Modeling

Yi Xie,[†,‡] Luigi Carbone,[§,‡,▽,*] Concetta Nobile,[§] Vincenzo Grillo,[⊥,||] Stefania D'Agostino,[†,#] Fabio Della Sala,[†,§] Cinzia Giannini,[△] Davide Altamura,[△] Christian Oelsner,[⊗] Carola Kryschi,[⊗] and P. Davide Cozzoli[§,¶,*]

[†]Center for Biomolecular Nanotechnologies@UNILE, Istituto Italiano di Tecnologia, Via Barsanti, I-73010 Arnesano (LE), Italy, [§]National Nanotechnology Laboratory (NNL), CNR Istituto Nanoscienze, c/o Distretto Tecnologico, Via per Arnesano km 5, I-73100 Lecce, Italy, [⊥]Centro S3, CNR Istituto Nanoscienze, Via Campi 213/A, I-41125 Modena, Italy, [||]IMEM-CNR, Parco Area delle Scienze 37/A, I-43124 Parma, Italy, [#]Dipartimento di Fisica, Università di Pavia, Via Bassi 6, I-27100 Pavia, Italy, [△]Istituto di Cristallografia (IC), CNR, Via Amendola 122/O, I-70126 Bari, Italy, [⊗]Department of Chemistry and Pharmacy and ICMM, Friedrich-Alexander University of Erlangen-Nuremberg, Egerlandstrasse 3, D-91058 Erlangen, Germany, and [¶]Dipartimento di Matematica e Fisica "E. De Giorgi", Università del Salento, Via per Arnesano, I-73100 Lecce, Italy. [‡]Y. Xie and L. Carbone contributed equally. [1]Present address: [▽]CNR IPCF, Via G. Moruzzi, I-56124 Pisa, Italy.

ABSTRACT In the realm of semiconductor nanomaterials, a crystal lattice heavily doped with cation/anion vacancies or ionized atomic impurities is considered to be a general prerequisite to accommodating excess free carriers that can support localized surface plasmon resonance (LSPR). Here, we demonstrate a surfactant-assisted nonaqueous route to anisotropic copper sulfide nanocrystals, selectively trapped in the covellite phase, which can exhibit intense, size-tunable LSPR at near-infrared wavelengths despite their stoichiometric, undoped structure. Experimental extinction spectra are satisfactorily reproduced by theoretical calculations performed by the discrete dipole approximation method within the framework of the Drude–Sommerfeld model. The LSPR response of the nanocrystals and its geometry dependence are interpreted as arising from the inherent metallic-like character of covellite, allowed by a significant density of lattice-constitutional valence-band free holes. As a consequence of the unique electronic properties of the nanocrystals and of their monodispersity, coherent excitation of symmetric radial breathing modes is observed for the first time in transient absorption experiments at LSPR wavelengths.

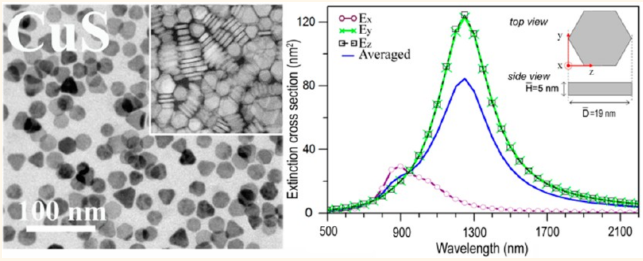

KEYWORDS: colloidal nanocrystals · copper sulfide · covellite · shape control · localized surface plasmon resonance · discrete dipole approximation · transient absorption spectroscopy

Colloidal heavily doped nanocrystals of metal chalcogenides and oxides represent an emerging class of functional nanoscale entities with dual semiconductor–plasmonic nature, which synergistically integrate the distinctive optoelectronic properties of low-dimensional semiconductors and localized surface plasmon resonance (LSPR) response.[1,2] The plasmonic behavior arises from collective oscillations of excess free carriers associated with constitutional vacancies or ionized dopant impurities in the lattice, leading to intense extinction bands at near-infrared (NIR) wavelengths.[1,2] In this realm, nanocrystals of nonstoichiometric copper chalcogenides ($Cu_{2-x}X$, with X = S, Se, Te) are especially convenient model systems for assessing the emergence of LSPR due to self-doping, as cation deficiency can be adjusted not only by selecting crystal phase and composition in the preparation stage[3−13] but also by performing postsynthesis red-ox[3,9,12,13] and cation-exchange reactions.[10,11] Control over structure and stoichiometry thus provides a useful tool for achieving dynamic, even reversible LSPR tunability through modulation of the free hole carrier density, an

* Address correspondence to davide.cozzoli@unisalento.it, carbone@ipcf.cnr.it.

Received for review June 16, 2013 and accepted July 16, 2013.

10.1021/nn403035s

opportunity prohibited to noble metal nanoparticle analogues, in which LSPR response is permanently locked in once geometric parameters (size and shape) have been engineered. $Cu_{2-x}X$ nanocrystals have already been proposed to be practically exploitable in biomedical imaging, photothermal cancer therapy, energy conversion and storage, and sensing.[1,14] However, full realization of their technological potential remains hindered by the elusive understanding of the detailed physical origin of LSPR and by the poor flexibility with which LSPR may be deliberately manipulated by rational material design. Several critical issues can, in fact, be identified, as follows.

Due to their rich phase diagrams, $Cu_{2-x}X$ nanocrystals can be trapped in a variety of copper-deficient polymorphs that, however, allow incorporating intrinsically low densities of cation vacancies.[4−13] In addition, the narrow structural stability domains of individual phases impose severe constraints to the stoichiometry deviations that may be tolerated when nanocrystals are forcedly subjected to chemical reactions aimed at compositional modifications.[5,12,13] These properties account for the modest levels of vacancy self-doping ultimately achievable and for the limited extent to which the free carrier concentration may be independently utilized as a tunable parameter for adjusting the LSPR.[5,6,12,13] Analysis of the ultrafast LSPR dynamics detected by transient absorption measurements has confirmed the remarkably lower free carrier density that may be accommodated in $Cu_{2-x}X$ nanocrystals, compared to that found in their noble-metal counterparts.[2,12,15] The difficulty to discriminate among different phases and their susceptibility to switch between uncertain compositions in response to mild changes in environmental conditions[5,6,12,13] complicate experimental assessment and decoupling of the individual effects of crystal structure, stoichiometry, and geometry on LSPR. On the other side, efforts to model the size dependence of steady-state LSPRs in near-spherical $Cu_{2-x}X$ nanocrystals have mostly relied on the use of the scattering theory in the quasi-static limit within the framework of the Drude−Sommerfeld model.[5,9,12,16] However, it has been pointed out that such an approach may be reasonably adequate only for metal nanocrystals and, thus, has to be taken with due reservation when applied to doped semiconductors, where carriers supporting LSPR may not behave as fully delocalized quantum oscillators.[11,16]

Knowledge on the plasmonic response of $Cu_{2-x}X$ nanocrystals with anisotropic morphologies, which are expected to support different LSPR modes and hence offer richer spectral tunability, is surprisingly sparse. The optical properties of nonspherical nanostructures accessed so far have in fact been examined over limited spectral ranges or even completely overlooked.[3,4,7,17−25] The few available exceptions denote the lack of clear consensus as to the shape dependence of spectral positions and relative intensities of the allowed LSPR modes.[6,11,13] In one of such reported cases, $Cu_{2-x}S$ nanodisks with chalcocite-to-digenite structure, obtained *via* a solventless thermolysis route, were claimed to exhibit two broad, asymmetric plasmonic bands peaking in the NIR (at 1600−1900 nm) and mid-IR (at >3200 nm) ranges.[6,13] These features were assigned as *out-of-plane* and *in-plane* dipolar LSPR modes, respectively, upon fitting the extinction spectra to a simple analytical expression based on an approximate nanocrystal shape and on the Drude model.[6,13] Spectral shifts observed under specified processing conditions were justified by invoking the competing effects of size and compositional changes on each LSPR.[13] Differently, another study documented a single, asymmetric extinction band in the NIR spectra of $Cu_{2-x}X$ nanorods obtained by a cation-exchange route.[11] Theoretical simulations performed by adopting different empirical and model phenomenological dielectric functions within the discrete dipole approximation (DDA) method clarified that the observed NIR feature resulted from the convolution of the *transverse* and *longitudinal* LSPRs, which were, in fact, predicted to lie close in energy and possess comparable intensities. Interestingly, this study highlighted that excess hole oscillators supporting LSPRs in $Cu_{2-x}X$ nanocrystals should be characterized by an essential degree of localization, in contrast with previous assumptions.[5,9,12,16]

The present work expands the available selection of plasmonic-active metal-chalcogenide semiconductor nanocrystals, demonstrating that a metal-deficient lattice does not always represent a stringent material requirement for generating LSPRs. We have focused on hexagonal covellite CuS, a stoichiometric member of the broad family of copper sulfides, which deserves special attention due to the particular crystal habit and unique metallic-like character accounting for its elevated, anisotropic p-type conductivity.[26−33] Although the exact bonding relationships and oxidation states (or charges) of its constituent atoms are still debated,[27,28,31,33−38] all proposed models of its electronic band structure suggest that CuS can intrinsically allow for a significant density of valence-band-delocalized holes without the need for intervening metal vacancies in the lattice.[39] Actually, CuS is inherently reluctant to incorporate cation vacancies due to the high activation energy required for their formation and the slow diffusion coefficient of cations within the lattice.[40−45] Thus, in nanostructured form, CuS holds promise as an unconventional vacancy-undoped copper-chalcogenide platform that could support composition-independent LSPRs exclusively correlating with its metallic-like nature and geometry.

As a major synthetic difficulty, reaction conditions that can ensure selective growth of covellite can be expected to be far more restrictive than those required for obtaining other phases, owing to its narrow thermodynamic stability domain.[46,47] In fact, despite the wealth of success in wet-chemical synthesis of nonstoichiometric

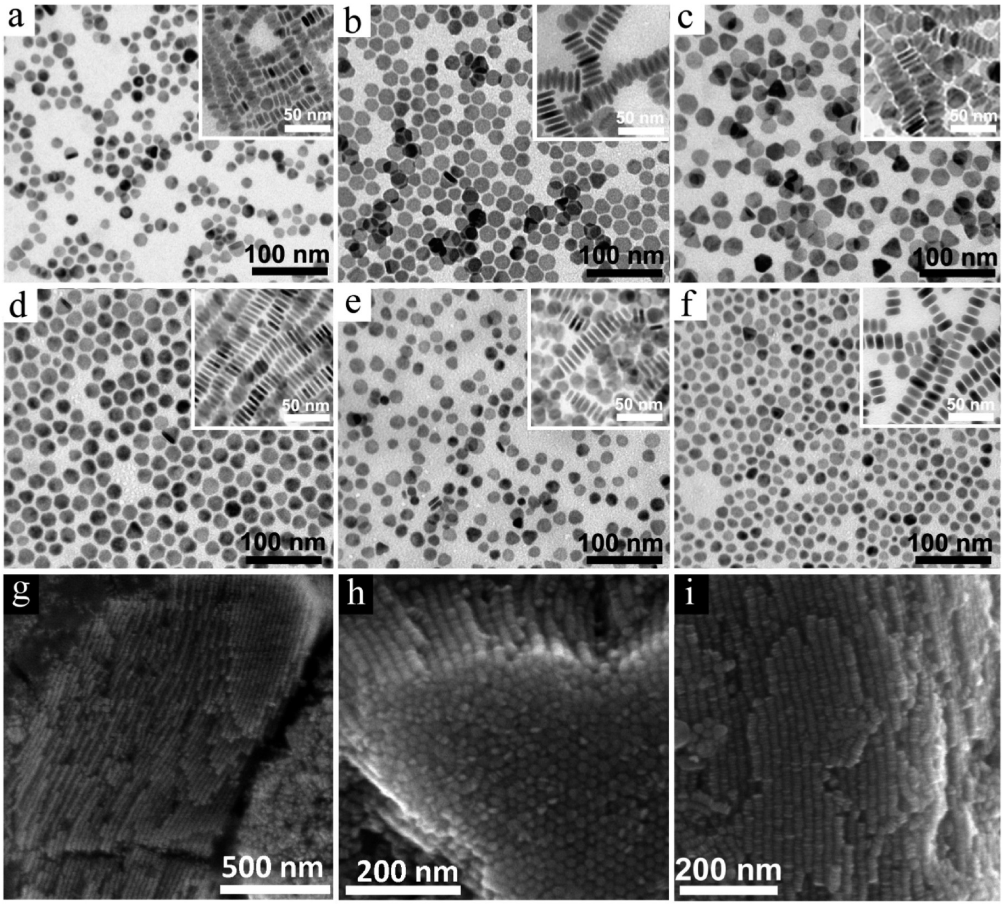

Figure 1. (a−f) Representative low-magnification TEM image galleries of CuS NDs synthesized in different environments at 180 °C: in OLAM/ODE mixtures at ODE:Cu molar ratios of 12:1 (a), 24: 1 (b), and 48:1 (c); in OLAM/OLAC/ODE mixtures at a fixed ODE:Cu molar ratio of 48:1 and at OLAC:OLAM molar ratios of 1:9 (d), 12:9 (e), and (f) 24:9, respectively. The respective insets show areas of the same samples where self-assembled ribbons of face-to-face stacked NDs are formed. (g−i) SEM images of different regions of a film of CuS NDs (corresponding to those shown in panel (c) deposited on a silicon substrate, where self-assembled ND superlattices made of dense-packed columns of face-to-face aligned ND stacks are clearly visible.

copper sulfides,[1,14] CuS nanocrystals have been documented rarely and their optical properties remain unexplored.[3,8,17,18,23,48]

Herein, we report on a colloidal approach for the phase-selective synthesis of monodisperse anisotropic CuS nanocrystals that can be tailored with two-dimensional disk-like shapes over a broad range of adjustable sizes. The nanodisks exhibit a single, intense extinction band at NIR wavelengths, which entails the convoluted contributions of a minority *out-of-plane* and a dominant *in-plane* dipolar LSPR mode. The experimental spectra have been satisfactorily reproduced and interpreted on the basis of DDA calculations performed within the framework of the Drude−Sommerfeld model. Combined experimental and theoretical analyses of the optical response of the nanodisks and its geometry dependence safely confirm the inherent metallic-like character of the stoichiometric covellite lattice of the nanocrystals. The high density of free hole carriers supporting LSPR ($\sim 10^{22}$ cm^{-3}) and the nanocrystal monodispersity account for the unprecedented detection of coherent excitation of symmetric radial breathing modes in transient absorption experiments at LSPR wavelengths.

RESULTS AND DISCUSSION

Nanocrystal Synthesis and Structural Characterization. We have developed a straightforward surfactant-assisted nonaqueous route through which monodisperse copper sulfide nanocrystals, distinguished by anisotropic disk-like shapes, can be selectively trapped in the covellite (CuS) crystal structure over a broad range of adjustable sizes. Our protocol relies on a one-pot, hot-injection technique, which involves the fast addition of a room-temperature S/OLAM solution to a suitably composed CuCl/OLAM/OLAC/ODE (copper chloride/oleyl amine/oleic acid/1-octadecene) mixture preheated at 180 °C under inert atmosphere, followed by a short annealing period. The level of size-morphological and crystal-phase control achievable can be appreciated from the representative low-magnification transmission electron microscopy (TEM)/scanning electron microscopy (SEM) galleries in Figure 1 and from the detailed structural analyses by X-ray diffraction

(XRD) and scanning TEM mode/high-resolution TEM (STEM-HRTEM) illustrated in Figure 2 and Figure 3, respectively.

In a monosurfactant OLAM/ODE environment containing fixed amounts of CuCl and OLAM, syntheses performed by varying the total ODE:Cu molar ratio from 12:1 to 48:1 yielded monodisperse hexagonal-shaped nanodisks (NDs) with a nearly constant average edge height (transverse axis), $\bar{H}$, of ~5 nm (size variance, σ_H < 10−15%) and mean base diameter (longitudinal axis), $\bar{D}$, systematically tunable from ~10 nm to ~28 nm (σ_D < 8−10%) (Figure 1a−c).

On the other hand, in binary OLAC/OLAM surfactant media, the reactions generated NDs, for which $\bar{D}$ could be progressively decreased from ~25 nm to ~10 nm and $\bar{H}$ was incremented from ~4.5 nm to ~8 nm, as the overall OLAC:OLAM molar ratio was regulated from 1:9 to 24:9 while keeping other conditions identical (ODE: OLAM = 24:9) (Figure 1d−f). In line with the trends just shown above, further modulation of $\bar{D}$ and $\bar{H}$ within the same size regime could be alternatively realized upon delicate adjustment of the precursor concentration combined with suitable regulation of the ODE content and the surfactant ratio.

The two-dimensional disk-like morphology of the nanocrystals could be unambiguously inferred on comparing the image contrast profiles diffracted by particles randomly oriented on the supporting carbon film of the TEM grid. Among these, NDs that were lying flat over the substrate projected shapes spanning from near-equilateral hexagons to truncated triangles, whereas NDs that were standing on their lateral sidewalls and exposed their basal facets parallel to the primary electron beam appeared as rod-like objects, the shorter and longer dimensions of which coincided with the transverse and longitudinal axis of the NDs, respectively (Figure 1a−g). As a consequence of their monodispersity and the particular platelet-like geometry, on one side, and of the favorable interparticle attractive forces enabled by the mixed capping shell of intercalated OLAM and ion-paired oleyl ammonium oleate species at the ND surface[49,50] (Figure S1 in the Supporting Information), on the other side, the NDs showed a natural tendency to spontaneously organize into ordered superlattices upon drop-casting from their colloidal solutions, followed by slow solvent evaporation. Isolated chain-like ribbons composed of base-to-base aligned NDs sitting over their edges formed already at low ND density, *e.g.*, on the TEM grid (top right insets in Figure 1a−f), while compact three-dimensional, close-packed micrometer domains accommodating columnar stacks of ND ribbons self-assembled from concentrated dispersions on solid substrates (Figure 1g−i).

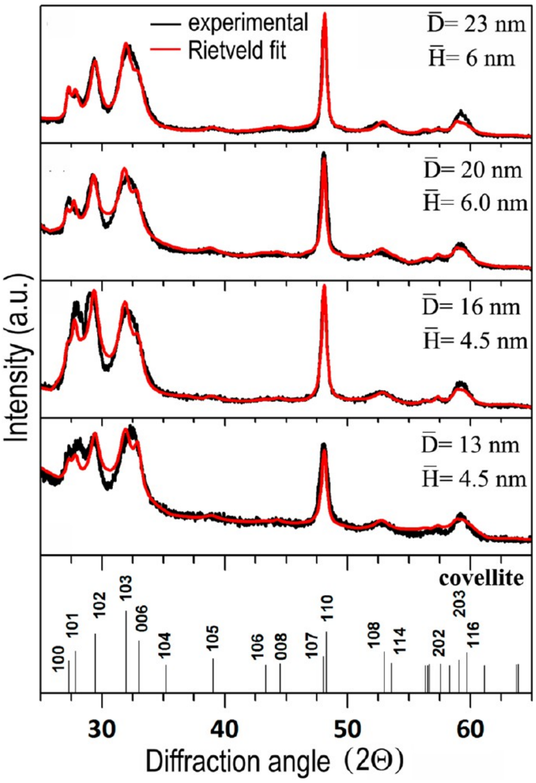

Figure 2. Experimental XRD patterns of variable-size CuS NDs (black points), along with the corresponding Rietveld-based fits (red traces) (see Table 1). The reference pattern of bulk stoichiometric covellite is marked on the bottom panel.

The XRD patterns acquired on dry powders of variable-size NDs (Figure 2) unambiguously substantiated the formation of nanometer-scale domains made of hexagonal-phase covellite with Cu:S = 1:1 stoichiometry. Quantitative analysis of the XRD data by means of a Rietveld-based fitting approach[51] corroborated the phase purity of the NDs with a weight percentage accuracy of ≤5−6% (note that the Cu:S molar ratio determined by inductively coupled plasma-atomic emission spectroscopy (ICP-AES) measurements ranged from 0.98 to 1.05, depending on the ND dimensions, which matched with the accuracy limits of the ICP-AES technique and the expected size-dependent surface enrichment in either element[5,9]). The covellite signature stayed invariant upon prolonged air exposure of the samples. Compared to the CuS bulk reference pattern, the samples typically exhibited reflections with inhomogeneous linewidths and altered intensity ratios, which evolved systematically with the nanocrystal dimensions. These features indicated anisotropic lattice development.[17,18,52] In particular, as the average volume and aspect ratio of the NDs increased, the (110) reflections (and, to a less perceivable extent, the (100) and (102) ones) became more prominent and sharp, while other signals, such as the (10*l*) (*l* = 4−7) and the (00*l*) (*l* = 6, 8), were comparatively attenuated. To interpret the size dependence of the patterns, the mean crystal-domain size of structural coherence along the most relevant low-index crystallographic orientations, D_{hkl}, was estimated by fitting the patterns through a Rietveld-based

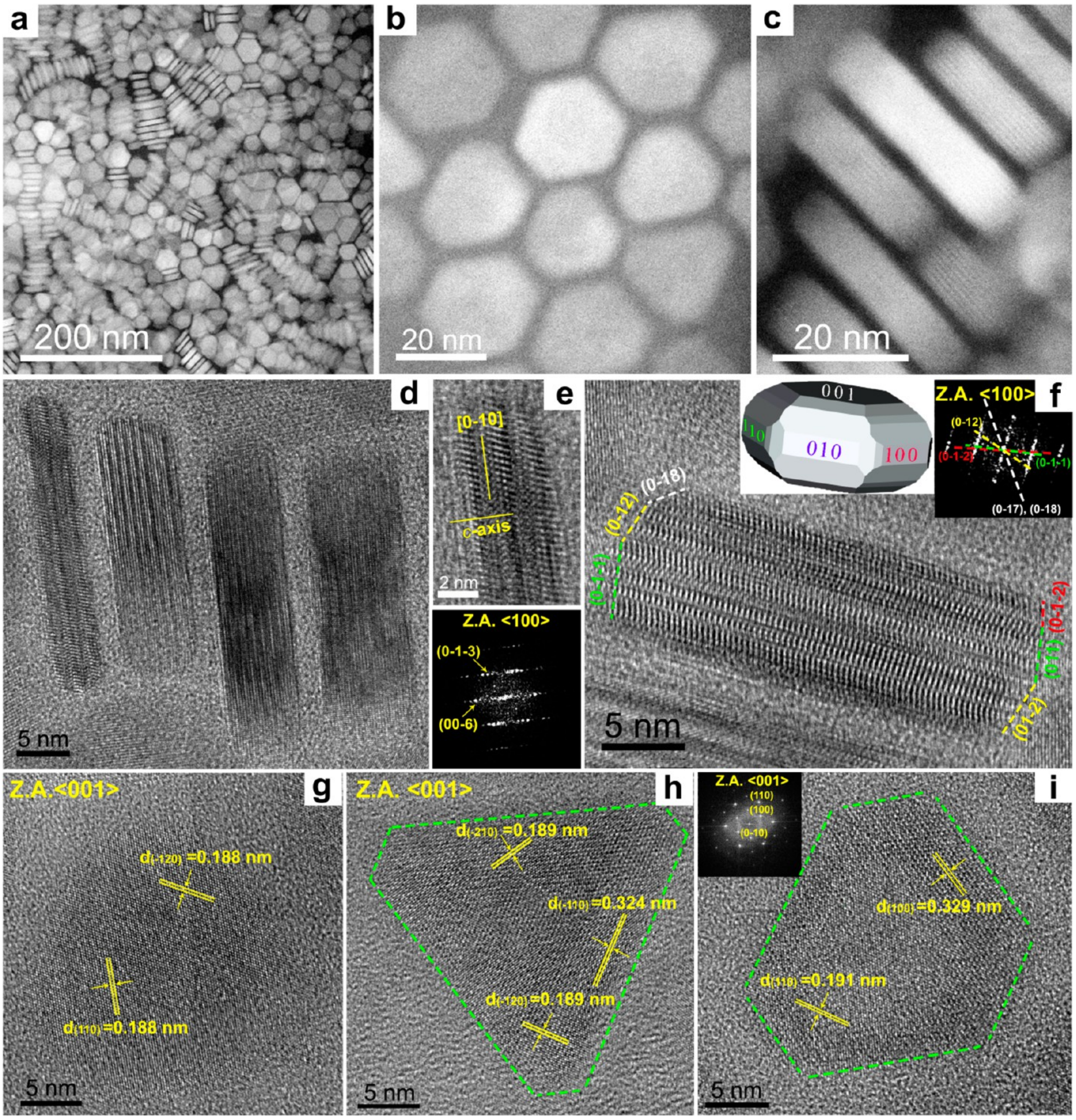

Figure 3. (a–c) ADF-STEM overviews of CuS NDs at variable magnification. (d–f) HRTEM images of ND groups and individual NDs lying with their shorter axis oriented parallel to the substrate; (g–i) HRTEM images of NDs with their major axis aligned parallel to the substrate, down the ⟨001⟩ zone axis. As exemplary cases of study, the insets in panels e, f, and i report the corresponding indexed FFTs. A sketch of the nanocrystal geometry, highlighting the hexagonal disk shape and complex faceting on the lateral sidewalls, has been added to panel f.

TABLE 1. Mean Coherent Domain Size, D_{hkl}, Estimated upon Rietveld-Fitting the XRD Patterns Shown in Figure 2

$\bar{D}$ (nm)[a]	$\bar{H}$ (nm)[a]	D_{110} (nm)[c]	D_{100} (nm)[c]	D_{006} (nm)[c]
13 ± 2	4.5 ± 0.5	15 ± 1	15 ± 2	8 ± 2
16 ± 2	5.5 ± 0.5	16 ± 1	16 ± 1	6 ± 1
20 ± 2	6.0 ± 0.5	20 ± 1	20 ± 1	6 ± 1
23 ± 2	6.0 ± 0.5	21 ± 1	22 ± 1	6 ± 1

[a] Mean sizes estimated by TEM by statistical analysis. [c] Minor discrepancies between the XRD-derived and TEM-measured sizes can be attributed to the presence of self-organized ND superstructures within the ND powders deposited on the silicon substrates for analysis. Micrometer-size domains of columnar face-to-face stacked NDs, in which the degree of intracolumnar ND ordering along the *c*-axis direction prevailed over the degree of intercolumnar alignment in the perpendicular orientations (Figure 1g–i), can be expected to hold higher structural coherence along the [001] and, to a lower extent, along the [010] and [110], relative to their fully disordered ND ensemble counterparts.

procedure relying on a phenomenological model that accounted for the inhomogeneous line broadening through a modified Scherrer formula[53,54] (see Materials and Methods section). According to the calculations, summarized in Table 1, increasingly larger and anisotropic NDs were characterized by systematically larger D_{110} and D_{100} (with $D_{110} \approx D_{100}$) and proportionally more modest D_{006} sizes. These analyses thus clarified that the ND lattice developed two-dimensionally along directions perpendicular to the *c*-axis. The satisfactory size correspondence between $\bar{D}$ and $\bar{H}$ estimated by TEM and the D_{110}/D_{100} and D_{006}, respectively, derived from the XRD data fitting (Table 1), anticipated the single-crystalline nature of the NDs.

Combined ADF (annular dark-field)-STEM and HRTEM studies provided a deeper insight into the composition, crystal structure, and geometry of individual nanocrystals (Figure 3).

In ADF-STEM imaging the brightness correlates with the local crystal thickness of the specimen along the primary electron-beam direction and with the average atomic number of the concerned material. NDs lying flat over the carbon film of the TEM grid exhibited a uniform contrast across their whole longitudinal profile (Figure 3a,b). Given that each ND possessed a constant size along its transverse axis, the observed ADF profiles substantiated their homogeneous chemical composition. In addition, the disk-like morphology of the nanocrystals could be indirectly inferred from the observation that the ADF intensity across the rod-like projections of individual base-to-base stacked NDs decreased along the two opposite directions from the central region toward the extremities (Figure 3a,c). At high resolution, continuous fringes could be recognized across the body of the NDs, which disclosed their monocrystalline nature (Figure 3c). Depending on nanocrystal orientation, the interparticle variation of the ADF brightness reflected the size variance associated with the ND heights and diameters, respectively, within the ND ensemble (Figure 3a−c).

HRTEM investigations, supported by fast Fourier transform (FFT) analysis of the relevant images, revealed that the NDs were single-crystalline objects, to which the hexagonal structure of covellite CuS could be univocally assigned on the basis of the identification of several sets of distinctive lattice fringes and of the angles among them (Figure 3d−i). Comparative examination of the lattice images of NDs viewed along different orientations allowed deciphering the relationships between the crystal structure and shape. The rod-like projections of base-to-base stacked NDs clarified that their shorter transverse axis possessed a uniform length and was aligned in the *c*-axis direction (Figure 3d−f). Accordingly, the flat top and bottom sides of the NDs were always composed of perfect (00 ±1) facets. Modulated fringes were frequently observed owing to stacking faults and/or dislocations along the [001].[17] Depending on nanocrystal size, the lateral surfaces of the NDs entailed combinations of the equivalent ±(010), ±(100), and ±(1−10) "prismatic" facets parallel to the *c*-axis and of "oblique" facets, *e.g.*, close to the ±(0−1−1), ±(0,−1,2), and (0,−1,8) planes (Figure 3f). On the other side, NDs lying flat on the grid, viewed down the ⟨001⟩ zone axis, projected two-dimensional hexagonal-shaped lattices delimited by peripheral edges perpendicular to the ±[010], ±[100], and ±[1−10] directions (Figure 3g−i). Taken together, these projections allowed deducing the coexistence of NDs with subtly dissimilar three-dimensional platelet shapes within the population, determined by a variable facet distribution along their lateral sidewalls (see sketch in the inset of Figure 3f). Namely, the samples should include (i) nearly regular hexagonal prisms enclosed exclusively by equally extended, prismatic facets; (ii) stretched tetradecahedrons enclosed only by oblique facets (each approximately composed of two highly truncated hexagonal bipyramids sharing a common (001) base); and (iii) stretched polyhedrons with mixed prismatic-oblique faceting. When viewed down the ⟨001⟩, the subfamily of hexagonal prismatic shapes would indeed generate equilateral-hexagonal profiles, while the other two families would project irregular, truncated-triangular profiles, respectively, in line with other observations (Figure 3g−1).

Growth Mechanism. ND evolution can be understood as resulting from a reaction dynamics that allows an adjustable nucleation−growth balance, across which selective generation and stabilization of the covellite phase under a continuous anisotropic development regime is guaranteed over a broad size range by suitable regulation of the chemical potential for the monomer species in the solution.

A CuCl/ODE/OLAM/OLAC mixture was initially preheated to 180 °C under an inert atmosphere. Due to coordination of CuCl to OLAM[55−57] and ODE ligands[58−61] *via* their amino and C═C double-bond moieties, respectively, the metal precursor present in the solution could be safely assumed to exist as neutral copper(I) oleylamino octadecene chloride complexes (hereafter referred to as $Cu_x(OLAM)_y(ODE)_zCl_x$), in equilibrium with free ODE and surfactant molecules, and ion-paired oleyl ammonium oleate species resulting from acid −base interaction of OLAM and OLAC.[49,50] The facts that OLAC alone was unable to solubilize CuCl and that the OLAM amount needed to dissolve CuCl was unaffected by the presence of OLAC discredited the possibility that the copper-based complexes could also entail carboxylate ligands. Accordingly, no contaminant copper oxide phases, which could in fact derive from OLAM-driven aminolysis of copper oleate species at moderate temperature,[62] were found (see also Figure S1 in the Supporting Information). Ultimately, the molecular structure and stoichiometry of $Cu_x(OLAM)_y(ODE)_zCl_x$ complexes should depend on the reaction composition, in turn, affecting their reactivity. In this regard it is interesting to note that no Cu(0) byproducts contaminating the synthesis product nor Cu(0) nanostructures were generated in our media in the absence of S. These pieces of evidence suggested that, most likely, CuS formation did not proceed *via* sulfidation of transient Cu(0) clusters formed upon Cu(I) reduction or disproportionation pathways, in contrast to what has been revealed for other systems.[23,57,63] Therefore, the aforementioned $Cu_x(OLAM)_y(ODE)_zCl_x$ complexes (or other secondary species thereof) could be regarded as acting as the actual Cu-based monomers sustaining CuS evolution under our synthesis conditions.

On the other side, the S/OLAM solution used to deliver the S precursor (in stoichiometric excess relative to Cu) contained oleylammonium polysulfides that could react with excess free amine under heating to generate various S-activated species, especially H_2S (trapped in the form of oleylammonium hydrosulfide) and, to a minor extent, thioamides.[64] At the temperature at which our syntheses were carried out, not only OLAM but also ODE could act as reducing agent for sulfur, contributing to supply extra H_2S.[65] Thus, *in situ* evolving H_2S molecules were the main S-based monomers feeding CuS growth.

On the basis of the chemistry highlighted above, the reaction dynamics underlying CuS ND formation can be rationalized. CuS formed upon direct reaction of $Cu_x(OLAM)_y(ODE)_zCl_x$ complexes with a stoichiometric excess of H_2S in ODE/OLAM/OLAC/oleyl ammonium oleate environment. Consistently, the final CuS NDs retained an organic capping shell made of a primary OLAM layer bound directly to the nanocrystal surface, which interacted with an outer layer made of intercalated free OLAM and oleyl ammonium oleate[49,50] (Figure S1 in the Supporting Information). This evidence suggested that OLAM should be the actual surface-active ligand that could affect nanocrystal growth upon binding to exposed Cu and S atoms.

Upon combination of the Cu and S monomers, the solution supersaturation abruptly increased beyond the critical threshold for condensation of CuS units to take place, resulting in a burst-like nucleation event. The hot-injection technique applied for delivering the S precursor, which allowed efficient reactant mixing and a provisional temperature drop, served as an effective technique for minimizing temporal overlapping of the nucleation and the growth stages, hence guaranteeing evolution of NDs with high size and shape monodispersity.[62] The nanocrystals developed very fast, reaching their full dimensions in a few minutes after injection, after which no further modifications were observed over time. This fact suggested that the NDs evolved in the absence of Oswald ripening, with the total amount of monomers utilized for building their lattice remaining constant. Under these conditions, size tunability is dictated by the established balance of monomer consumption between the homogeneous nucleation and growth stages, as governed by the nucleation rate.[62] The greater the concentration of nuclei that are initially generated, the proportionally lower the monomer concentration left in the solution for which the embryos will have to compete. Consequently, the nuclei will grow only to comparatively smaller dimensions. The size trends obtained in our syntheses can thus be understood by analyzing the impact of the reaction composition on the nucleation extent.

The outcome of the OLAC-free syntheses, in which gradually higher ODE:Cu molar ratios led to systematically larger NDs (Figure 1a−c), indicated that the nucleation burst was increasingly mitigated. This implied that the initial relative supersaturation degree realized in the reaction mixtures was attenuated. It follows that the contribution of the enhanced H_2S chemical potential enabled by the larger availability of S-activating agents (namely, ODE or OLAM) should be largely overwhelmed by the opposite effect of a decreased reactivity and/or diffusivity of the $Cu_x(OLAM)_y(ODE)_zCl_x$ complexes. Such an altered property could stem partly from the higher dilution and partly from induced changes in the structure and/or stoichiometry of the complex.

On the other hand, the results of OLAC-assisted syntheses, which allowed access to gradually smaller NDs (Figure 1d−f), suggested that the nucleation event was boosted on increasing the relative OLAC content. In such cases, shifts of the relevant equilibria toward formation of oleyl ammonium oleate should correspond to a reduced availability of OLAM for stabilization of the $Cu_x(OLAM)_y(ODE)_zCl_x$ complex. This condition could enhance the reactivity of the latter, compensating for the opposite impact of the higher Cu-precursor dilution and of reduced availability of S-activating species.

After nucleation, the crystal structure in which the embryos were formed (Figure 2) drove their evolution to the observed disk-like shapes. Low-symmetric hexagonal covellite CuS, characterized by a pseudographitic structure with alternating $CuS_3-Cu_3S-CuS_3$ layers and S−S layers along the [001],[17] can be indeed expected to exhibit an intrinsic propensity to develop anisotropically either along or perpendicular to its unique *c*-axis of high symmetry. The detailed geometry and particular faceting associated with the variety of hexagonal disk shapes observed in our ND samples (Figure 3d−i) indicate that, under our synthesis conditions, lattice growth was slowed along the [00±1] directions, most likely due to the high stability (hence, low reactivity) of the corresponding (00±1) surfaces, while it proceeded much faster in the ±[010], ±[100], and ±[1−10] directions, thereby accounting for the general tendency toward adoption of a two-dimensional habit. As NDs developed extended (00±1) basal facets, more unstable prismatic and oblique facets competed in accumulating on the lateral sidewalls in variable relative proportions, because of their higher, yet comparable surface energies. Anisotropic growth could be further promoted by dynamic facet-preferential adhesion of OLAM and by the soft templating action played by oleyl ammonium oleate couples interacting with the primary OLAM layer.[49,50]

The selective trapping of the NDs in the covellite structure deserves further remarks.

For a nanocrystal the total free energy of formation is given by the sum of a volume-energy term (the energy gained when solution monomers are incorporated in the growing nuclei) and a surface-energy term (the energy that must be spent to create new solid/solution interfaces). While the former contribution depends on the chemical potential of the solution monomers and its time evolution, the latter is dictated by the nanocrystal geometry and the presence of surface-adhering ligands or surfactant. This could lead to a size and shape dependence of the relative stability order of the possible polymorphs that may form, as verified for other material systems.[62]

According to the experimental and calculated thermodynamic databases for the bulk Cu–S system at ambient pressure,[46,47] covellite CuS and liquid S are expected to be equilibrium phases at temperatures of 120 °C < T < 500 °C only in the S-rich region of the Cu–S phase diagram, whereas solid Cu(0) and nonstoichiometric $Cu_{2-x}S$ phases should become increasingly preferred at higher temperatures and/or Cu-rich compositions. Thus, critical to determining thermodynamic selection of covellite over other copper sulfide polymorphs is the identification of phase-specific chemical-potential and surface-energy domain by suitable adjustment of the reaction environment and temperature.

Our protocol afforded CuS NDs with tunable sizes upon reacting CuCl with S at a S:Cu molar ratio of 4:1 in OLAC:OLAM:ODE media at 180 °C. At lower temperatures nucleation and growth were significantly slowed. Increasing the reaction temperatures from 180 °C up to 270 °C led to the samples characterized by irregular platelet shapes and mixed phase compositions, in which covellite CuS coexisted with gradually larger fractions of digenite $Cu_{1.95}S$ and low-chalcocite Cu_2S. Accordingly, the Cu:S molar ratio measured by inductively coupled plasma atomic emission spectroscopy (ICP-AES) increased steadily from 1.05 to 1.91 (Figure S2 in the Supporting Information). Our results thus indicated that the particular OLAC:OLAM:ODE media in which copper sulfide nanocrystals were generated from CuCl and excess S guaranteed growth conditions preserving the same relative phase stability order as that predicted for the bulk Cu–S system. In this respect, CuS may be regarded as a thermodynamically controlled product, although specific kinetic factors could also favorably come into play in its formation. It is worth noting, however, that the temperature range over which nanocrystal nucleation and growth could switch from covellite CuS to other crystal structures was much narrower and shifted to significantly lower values than those found for the bulk. This fact revealed that the surface energy contribution impacted significantly on the total free energy of nanocrystal growth in the selected OLAC:OLAM:ODE media. Due to the nanoscale effect, the free energies of formation of the possible copper sulfide polymorphs could be raised to a variable extent (a lowering of the respective melting points should correspondingly be expected[62]), yet ranking within the same energy sequence as that expected for the respective bulk phases. This could ultimately lead to smaller differences in thermodynamic stability among the possible polymorphs, thus making reaction temperature the most influential phase-discriminating synthesis parameter.

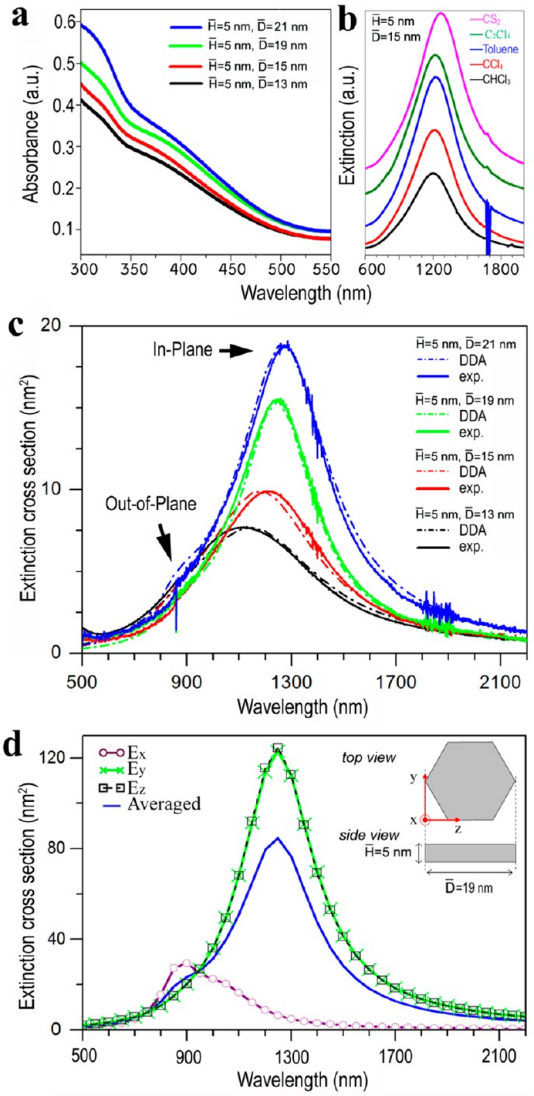

Figure 4. Optical properties of variable-size CuS NDs. (a) Absorption spectra in the UV–vis region of NDs in CCl_4. (b) Typical solvent dependence of the NIR extinction of an ND sample. (c) NIR extinction spectra of NDs in CCl_4 (continuous lines), along with the corresponding DDA-based fits (dashed lines) (see Table 2). Note that the DDA-fitted spectra were *normalized* to the corresponding experimental extinction band maxima. (d) Computed DDA extinction scattering cross sections of an ND ($\bar{H}$ = 5 nm, $\bar{D}$ = 19 nm for ω_p = 4.5 eV, ε_∞ = 9 and γ = 0.25 eV), calculated for incident light polarized along the transverse (x)- and longitudinal-axis directions (y, z) and with orientational averaging.

Steady-State Optical Properties. Figure 4a–c reports the experimental UV–vis–NIR extinction spectra of solution samples of NDs characterized by comparable transverse axis $\bar{H}$ (~5 nm) and by variable $\bar{D}$. The broad absorption shoulder occurring in the UV-blue region below ~550 nm (Figure 4a) was related to excitonic transitions across a direct band gap of about 2.2–2.4 eV, as previously estimated for covellite.[3–6,8,12,13,16,29,66] In nanostructured copper sulfides band gap variation

TABLE 2. Parameters Featuring the Steady-State NIR Extinction of the Variable-Size CuS NDs (dissolved in CCl_4; refractive index = 1.4601), Deduced on the Basis of DDA-Based Calculations and Fits of Experimental Spectra in Figure 4c

$\bar{D}$ (nm)[a]	$\bar{H}$ (nm)[a]	λ_{max}^{exp} (nm)[b]	λ_{max}^{DDA} (nm)[c]	λ_{in}^{DDA} (nm)[d]	λ_{out}^{DDA} (nm)[e]	ε_∞[f]	ω_p(eV)[g]	γ (eV)[h]	$\Delta\sigma$ (%)[i]
13 ± 2	5.0 ± 0.5	1112	1144	1168	954	9	4.5	0.5	3.1
15 ± 2	5.0 ± 0.5	1211	1181	1194	923	9	4.5	0.4	3.3
19 ± 2	5.0 ± 0.5	1245	1245	1248	891	9	4.5	0.25	2.1
21 ± 2	5.0 ± 0.5	1276	1266	1274	888	9	4.5	0.3	1.6

[a] Mean sizes estimated by TEM by statistical analysis. [b] Wavelength corresponding to the maximum NIR extinction band in the experimental spectra in Figure 4c. [c] Wavelength corresponding to the maximum NIR extinction band in the DDA spectra calculated including orientational averaging. [d] Wavelength corresponding to the maximum NIR extinction in the DDA spectrum calculated for incident field polarized along the ND longitudinal axis (in-plane LSPR). [e] Wavelength corresponding to the maximum NIR extinction in the DDA spectrum calculated for incident field polarized along the ND transverse axis (out-of-plane LSPR). [f] Constant taking into account the polarization background of the ion cores. [g] Drude plasma frequency. [h] Damping constant. [i] Relative difference between the DDA-calculated and experimental extinction cross sections.

depends on both quantum confinement, which has been predicted to set in the sub-10 nm regime,[3,66] and the Moss–Burstein effect.[3,5,12,66] The absorption onset of the NDs appeared to be independent of the ND size, since the band gap was dictated by the crystal structure of stoichiometric covellite and the shortest-confined dimension, $\bar{H}$, both of which were identical for all samples.

In the 600–2200 nm region (Figure 4b,c), the spectra entailed a prominent, isolated band, characterized by slight asymmetry emerging on the higher-energy side for relatively larger ND sizes. Such a band expressed the genuine NIR properties of diluted ND ensembles, as dynamic light scattering analyses (not shown) confirmed that the samples did not contain particle aggregates that could affect spectrophotometric measurements. No extra spectral features were recognized at lower energies up to the wavelength limit accessible by our instrumentation as well as in the mid-IR region by Fourier transform infrared spectroscopy (FT-IR) measurements (Figure S1 in the Supporting Information).

Several observations highlighted the strong similarity between the optical behavior of our NDs and the typical response of plasmonic-active metal and heavily doped semiconductor nanocrystals dispersed in liquid media. First, the measured extinction cross section fell in the 5–20 nm^2 range, accounting for molar absorptivities comparable to those of noble-metal nanocrystals (Figure S3 in the Supporting Information). Second, as $\bar{D}$ was tuned from ~13 nm to ~22 nm, the wavelength at the extinction maximum, λ_{max}^{exp}, increased from ~1112 nm to ~1276 nm (Table 2), accompanied by an increase in band intensity and gradual narrowing of the peak line width (Figure 4c, solid lines). Third, the NIR band red-shifted and grew with increasing refractive index of the solvent (Figure 4b), whereas the excitonic feature remained unaltered. Taken together, all these experimental pieces of evidence corroborated the LSPR origin of the NIR extinction exhibited by the CuS NDs. The NIR resonance was characterized by a good quality factor (defined as the ratio of λ_{max}^{exp} to the LSPR line width)[67] of >3, which should reflect not only the tight size distribution but also the compositional homogeneity within the ND population of individual samples.[2,5,8,12]

To understand the above results, it is useful to recall that in plasmonic $Cu_{2-x}S$ nanocrystals the free hole carriers underlying LSPR originate from copper deficiency accommodated in crystal phases that can individually exist within narrow ranges of chemical and structural stability.[4–10,12,13,66] In contrast, the LSPR of the present CuS NDs stems from lattice-constitutional free holes that are inherently allowed by the unique electronic configuration associated with stoichiometric covellite.[39] According to our observations, the CuS NDs were chemically and structurally stable under ordinary processing conditions, confirming the known negligible susceptibility of bulk covellite toward incorporation of copper vacancies *via* cation extrusion or exchange under a variety of conditions.[40–45] Indeed, unlike their $Cu_{2-x}S$ counterparts,[5,12,13] the CuS nanodisks could withstand prolonged exposure to air in their synthesis medium or in other solvents even at moderate temperature, retaining their crystal structure, size, shape, and pristine optical features. Actually, CuS cannot tolerate deviation from its unique Cu:S = 1:1 stoichiometry, as any alteration in composition *via* forced oxidation under harsh conditions would inevitably result in undesired phase transformation.[40–45] These facts further guaranteed that the LSPR features of the NDs were exclusively governed by their geometric parameters, as the constitutional free hole density underlying the LSPR was univocally set by the particular composition and crystal structure of stoichiometric covellite.

Another aspect deserving remark concerns the single LSPR feature generated by our CuS NDs. Our data would seemingly contrast with the expectation that nanocrystal shape anisotropy should, in principle, lead to multiple scattering peaks. In the case of plasmonic noble-metal nanocrystals with two-dimensional habits, at least two distinct bands, corresponding to the out-of-plane and in-plane dipolar LSPRs, respectively, are commonly detected.[68–70] In a recent study, $Cu_{2-x}S$ NDs with chalcocite-to-digenite structure have also been claimed to support two broad LSPRs with large energy separation.[6,13] In contrast, a single LSPR band was assessed for $Cu_{2-x}X$ nanorods and explained as resulting from the strong overlapping of transverse and longitudinal LSPRs.[11] As to the present case, the variation of $\lambda_{\max}^{\exp}$ as a function of the ND dimensions (Figure 4c), which followed a trend opposite that observed for near-spherical $Cu_{2-x}S$ nanocrystals,[5,12] instead matched with the characteristic behavior of the in-plane dipolar LSPR supported by platelet-like metal nanocrystals, such as of Ag.[68−70] For such shaped nano-objects, the in-plane LSPR corresponds to the most prominent, lowest-frequency NIR band and is indeed expected to red-shift and shrink with increasing aspect ratio, as indeed verified in our case. On the other side, the frequencies at which the out-of-plane and in-plane LSPRs resonate in the CuS NDs may diverge to a small extent from one another with increasing the particle aspect ratio, compared to what occurs in plasmonic noble-metal nanocrystals.[11,69,70] On the basis of the observations above, we could provisionally attribute the NIR band to in-plane LSPR mode and assume that other plasmonic features expected at higher frequency, such as the out-of-plane LSPR mode, remained unresolved due to their small energy separation and/or the comparatively much lower intensity.[11]

Theoretical Modeling of Steady-State NIR Spectra and Assignment of the LSPRs. To support the preliminary interpretation of the optical properties of the NDs given above, the experimental NIR spectra were rationalized on the basis of electrodynamic scattering simulations performed within the frame of the discrete dipole approximation.[71−73] This method allows calculating the extinction coefficient of nanocrystals of arbitrary geometry by solving the relevant Maxwell's equations. According to the DDA main approximation, the target sample that interacts with an incident light wave is treated as a finite array of interacting point dipoles with polarizabilities described by the effective "bulk" dielectric function, $\varepsilon(\omega)$, of the material. Multiple LSPR modes arising from shape anisotropy can be straightforwardly predicted and identified. The DDA approach enabled accurate modeling of the actual prismatic habit of the CuS NDs to faithfully reproduce the experimental spectral features.

The complex dielectric function, $\varepsilon(\omega)$, was expressed as a function of the frequency, ω, by using the Drude−Sommerfeld model:[5,15,16]

$$\varepsilon(\omega) = \varepsilon_\infty - \frac{{\omega_p}^2}{\omega^2 + i\gamma\omega} \qquad (1)$$

where ε_∞ takes into account the polarization background of the ion cores, γ is the damping constant (or collision frequency), and ω_p is the Drude plasma frequency related to the density of free carriers (holes), N_h:

$$\omega_p = \sqrt{\frac{N_h e^2}{\varepsilon_0 m_h}} \qquad (2)$$

where ε_0 is the vacuum dielectric constant, e is the electron charge, and m_h is the hole effective mass (assumed to be equal to unity).

In our calculations, ω_p was imposed to be independent of the ND volume, which transcribed the hypothesis of nanocrystals featured by equal crystal structure and composition at all sizes, consistent with our XRD and HRTEM analyses. Differently, due to the small particle dimensions, γ is expected to decrease with the nanocrystal size due to free carrier collisions with the nanocrystal surface (surface damping).[74] In the case of spherical nanocrystals, a common approximation used is $\gamma = \gamma_0 + A/R_{NC}$, where γ_0 is the damping constant for the free holes in the bulk, A is a constant accounting for the Fermi velocity and scattering events with the surface, and R_{NC} is the nanocrystal radius. More accurate models are available to express γ associated with complicated shapes.[74] In the present case, γ was simply allowed to change with the $\bar{D}$ of NDs. Concerning the high-frequency limit, ε_∞, it is also related to the scattering and includes the contribution of the bound carriers to the polarizability. However, the value of ε_∞ is unknown, although it has often been taken as 1 for copper chalcogenides under the assumption that only valence-band holes may affect the dielectric function.[5,6]

Our aim was to extract ε_∞, ω_p, and γ by fitting the experimental spectra. To this purpose, the relative difference ($\Delta\sigma$) between the DDA-calculated and experimental extinction cross sections of variable-size NDs (dissolved in CCl_4) was minimized through a three-dimensional scan of the ε_∞, ω_p, and γ parameters (see Materials and Methods section). Four samples of NDs (with $\bar{D}$ = 13, 15, 19, 21 nm and $\bar{H}$ = 5 nm) were simultaneously considered. Importantly, the calculations included, for each sample, orientational averaging, which is (albeit computationally expensive) essential to correctly account for the effect of the anisotropic nanocrystal shape and of different polarizations of the incident wave on light absorption and scattering.

The absolute minimum, $\Delta\sigma$ = 2.5%, was found for ε_∞= 9 and ω_p = 4.5 eV. The corresponding values of γ as well as of $\Delta\sigma$ for each ND sample are listed in Table 2. The optimized computed spectra, displayed in Figure 4c (dashed curves), illustrate the excellent agreement between the experimental and the fitted extinction data. The sampling error was estimated to be around 2% (see Materials and Methods section); thus the obtained minimum of $\Delta\sigma$ = 2.5% was close to the numerical accuracy. Note, however, that a comparably high degree of fit accuracy ($\Delta\sigma$ < 3%) could be achieved from other sets of parameters (*e.g.*, ε_∞ = 7 and ω_p = 4.3 eV, or ε_∞ = 11 and ω_p = 4.7 eV). Thus, the available experimental data could not allow a more precise determination of ε_∞, as interband transitions are likely to occur at λ < 500 nm, where the Drude model (eq 1) is highly inaccurate. Thus, in the NIR region, decreasing ω_p will lead to a red-shift of the LSPR band in a way similar to increasing ε_∞ (Figure S4 and Figure S5 in the Supporting Information).

From the fits in Figure 4c and the fit parameters in Table 2, the following conclusions were drawn.

First, the fits substantiated the distinct electronic properties of the CuS covellite phase in which our NDs were trapped and the peculiar origin of the carriers sustaining the near-infrared LSPR. Namely, the high DDA fit quality demonstrated that the Drude–Sommerfeld model was accurate enough to describe the behavior of the carriers generating the LSPR in all samples. This implied that the NDs should hold a genuine metallic-like electronic structure allowing inherently free hole carriers, delocalized within the valence band. In this respect, the present CuS NDs diverge from their $Cu_{2-x}X$ counterparts reported so far, in which valence-band holes supporting LSPRs are indeed characterized by a substantial degree of localization.[11]

The value of ω_p = 4.5 eV extracted from the fit (Table 2) corresponds to $N_h \approx 0.98 \times 10^{22}$ cm^{-3} (*i.e.*, ~0.32 holes per CuS molecular unit), which approaches the free carrier concentration typical of several metals.[27−32,34] Thus, the CuS NDs were found to accommodate a free hole density ~7 to ~13 times higher than that deduced for $Cu_{2-x}S$ nanocrystals with $1.93 < 2-x < 2$ ($N_h \approx (0.77-1.36) \times 10^{21}$ cm^{-3}), for which the ultimate self-doping level achievable is severely limited by their narrow structural stability window.[5,6,13,12,16] In this regard, it is worth recalling that such previous estimations of N_h in $Cu_{2-x}S$ nanocrystals are likely to be imprecise, as the Drude–Sommerfeld model assumed in Mie theory analysis of the relevant extinction spectra fails to account for the actual (*i.e.*, partially localized) character of hole carriers sustaining LSPR in those nonstoichiometric materials.[11,16] On the other hand, the N_h deduced for our NDs would fall far below the hole density that should be admitted if their constituent CuS were misinterpreted as a hypothetical $Cu_{2-x}S$ phase featured by a large cation deficiency corresponding to $2 - x = 1$. The estimated N_h of the CuS NDs is realistic, consistent with the metallic conductivity of bulk CuS.[26−28,31,34] It is not surprising that N_h even exceeds the level determined by Hall coefficient and resistivity measurements on polycrystalline CuS thin films ($N_h \approx 1.8 \times 10^{20} - 1.7 \times 10^{21}$ cm^{-3}),[26,27,29,32] where the presence of foreign amorphous or crystalline phases, inhomogeneity in microstructure, and defects can, in fact, reduce the ultimate material conductivity.

Taken together, all observations above confirmed the expectation that the NDs did not sustain LSPR through a mechanism of vacancy self-doping, analogous to that assessed for other nonstoichiometric metal chalcogenide and oxide materials.[5−10,12,13] Rather, the DDA-deduced ω_p should be regarded as further corroborating the inherent metallic-like p-type nature of the CuS NDs, enabled by a large availability of valence-band delocalized (Drude-type) holes that are constitutional in stoichiometric covellite[27,28,31,33−39] and cannot in fact be forcedly introduced without disrupting the hexagonal lattice.

Second, the satisfactory convergence of the fitting procedure indicated that the optical properties of all samples could be reliably reproduced through a single ω_p value, implying that the NDs accommodated similar free carrier density regardless of their dimensions. Besides validating the initial hypothesis of a size independence of the composition and structure of the obtained copper sulfide phase, this result clarified that the tunability of the achieved LSPR response was entirely governed by the ND geometric features.

Third, the DDA calculations revealed that the prominent NIR extinction band resulted from the convolution of two unresolved features: a major contribution from the in-plane dipolar LSPR at λ_{in}^{DDA} and a minor contribution from the out-of-plane dipolar LSPR resonating at λ_{out}^{DDA} on the higher-energy side of the NIR feature, as exemplified in Figure 4d. The experimental λ_{max}^{exp} closely matched with λ_{in}^{DDA} as well as with λ_{max}^{DDA}, the wavelengths corresponding to the NIR extinction maxima in the DDA spectra calculated including orientational averaging (see Table 2). The calculations suggested that, due to the small energy separation of λ_{in}^{DDA} and λ_{out}^{DDA}, and the comparatively lower intensity of the out-of-plane LSPR, the latter resonance could produce a minor, hardly recognizable bump-like feature only in the spectrum of the larger aspect ratio NDs, in good agreement with the experimental data (*cf.* Figure 4c and d). A similar weak size dependence of the spectral positions of two main allowed transverse and longitudinal LSPRs, and a significant damping of the longitudinal mode, compared to those found in their noble-metal counterparts, was also deduced for $Cu_{2-x}X$ nanorods with partially localized oscillating holes.[11] However, in the present case, the large intensity difference and small energy separation between the in-plane and out-of-plane LSPRs of the CuS NDs have a clearly different physical origin. The strong in-plane LSPR exhibited by the NDs is in fact characteristic of plasmonic platelet-shaped nanocrystals accommodating Drude-like (*i.e.*, fully delocalized) carriers.[69,70] In addition, it should be considered that hole conductivity in CuS is strongly anisotropic.[26−28,34] Recent first-principles calculations have indicated that the in-plane (*i.e.*, perpendicular to the *c*-axis) plasma frequency is significantly higher than the out-of-plane one.[31] This property implies that, compared to their shaped noble-metal nanocrystal analogues, characterized by isotropic ω_p, the out-of-plane LSPR band of CuS NDs should be expected to fall at longer wavelengths (thus, approaching the in-plane LSPR) and exhibit a further reduced intensity, in agreement with our experimental evidence.

TABLE 3. Physical Parameters Featuring the LSPR Dynamics of Variable-Size CuS NDs, Extracted upon Fitting the TA Spectra in Figure 5

$\bar{D}$ (nm)[a]	$\bar{H}$ (nm)[a]	σ_D (nm)[b,f]	bleaching maximum wavelength (nm)[c]	T (ps)[d,f]	τ (ps)[e]
13 ± 2	5.0 ± 0.5	0.90 ± 0.01	1140 ± 1	5.10 ± 0.10	8.10 ± 0.12
15 ± 2	5.0 ± 0.5	1.10 ± 0.01	1210 ± 1	5.70 ± 0.13	8.90 ± 0.13
19 ± 2	5.0 ± 0.5	1.70 ± 0.02	1240 ± 1	7.00 ± 0.15	8.90 ± 0.16
21 ± 2	5.0 ± 0.5	1.80 ± 0.02	1260 ± 1	7.70 ± 0.20	10.00 ± 0.20

[a] Mean sizes estimated by TEM by statistical analysis. [b] Standard deviation of the ND sample. [c] Parameter measured directly from TA spectra in Figure 5a–d at a delay time of 0.5 ps. [d] Period of the oscillation. [e] Damping time. [f] Parameters estimated by fitting the experimental TA kinetic traces to eq 3 and averaging the values calculated from 10 kinetic traces.

On the basis of all these arguments, the result of our DDA calculations overall demonstrated that the Drude–Sommerfeld picture was indeed adequate to describe the behavior of hole carriers supporting the LSPRs in CuS: like their noble-metal nanodisk analogues, CuS NDs with a fixed thickness $\bar{H}$ and constant density of delocalized carriers exhibited a dominant in-plane LSPR band for which $\lambda_{\text{in}}^{\text{DDA}}$ red-shifted with increasing $\bar{D}$ and a much weaker out-of-plane LSPR feature for which $\lambda_{\text{out}}^{\text{DDA}}$ followed an opposite size trend[69,70] (see Table 2).

Ultrafast LSPR Dynamics. Further proofs in favor of the metallic-like electronic properties of the CuS NDs were gathered from analysis of their ultrafast LSPR dynamics. To this purpose, the optical response of the NDs to ultrashort (150 fs) laser pulses (387 nm) was recorded in pump–probe transient absorption (TA) spectroscopy experiments at variable pump fluencies. The most relevant physical parameters deduced from TA data analysis are listed in Table 3. Figure 5a–d reports the typical time evolution of the change in the optical density (ΔOD) of solutions of CuS NDs with comparable $\bar{H}$ and different $\bar{D}$. The TA spectra showed a negative ΔOD around the LSPR wavelengths and a positive ΔOD at lower energies, both of which tended to vanish within a few picoseconds. The positions of the negative maxima exhibited a pronounced dependence on $\bar{D}$ (Table 3) and were blue-shifted relative to the LSPR maxima recorded in absorption mode to an extent (∼10 to ∼60 nm) that decreased at progressively longer delay times. These results can be understood on considering that, in a TA experiment, optical excitation of metal or metallic-like nanocrystals stimulates dipolar oscillations of the free charge carriers that dephase within tens of femtoseconds. In particular, pump laser pulses with energy much higher than that corresponding to the LSPR may induce instantaneous interband transitions, which create a nonthermal distribution of "hot" charge carriers. Then, dephasing of the LSPR occurs as the hot carriers rapidly equilibrate *via* intrinsic damping pathways (bulk or carrier-surface scattering), leading to a Fermi distribution at a higher carrier temperature.[75] Such a thermalization process generates a photoinduced bleaching (PIB) of the ground-state population density and photoinduced absorption (PIA) due to transitions of excited species.[76] These processes should then result in a negative band in proximity to the LSPR and a positive absorption at longer wavelengths, as actually detected by us. Since the time constant of the carrier–carrier scattering process scales with the nanocrystal dimensions,[75–77] the observed size dependence of the PIB maxima was indeed expected. The blue-shift of the maxima positions could reasonably arise from the superimposition of the ground-state PIB with the PIA emerging therewith at lower energies.

The transient PIB and the PIA features decay on the time scale of a few picoseconds as the hot-carrier distribution relaxes *via* phonon emission (with the carrier–phonon scattering time constant increasing with the laser pump fluence) and subsequent phonon–phonon scattering, ultimately dissipating heat into the solvent. Importantly, the carrier–phonon coupling causes an instantaneous increase in the lattice temperature, which leads to a change in the equilibrium volume of the nanocrystals by a percentage extent proportional to $\alpha\Delta T_{1att}/3$, where α is the thermal expansion coefficient and T_{latt} is the lattice temperature.[75] In the case of ultrafast laser pulse excitation, the time scale over which the lattice is heated (*ca.* 1 ps) is much shorter than that of lattice dilatation. This triggers impulsive excitation of coherent vibrational (breathing) modes, *i.e.*, oscillations of the nanocrystal volume, which then decay upon acoustic energy transfer to the environment. Therefore, the induced breathing mode may affect the behavior of the transients since the nanocrystal volume changes associated with the vibrational motion may modify the surface plasmon resonance condition.[75,76]

Figure 5e–h presents exemplary TA kinetic traces (transients) that were derived by following the TA signal at individual wavelengths (see dotted lines). The decays exhibited clear harmonic modulations over the whole range of detection wavelengths, except for the spectral region around the bleaching maximum (see, for example, the trace detected at 1200 nm for the NDs with $\bar{D}$ = 15 nm in Figure 5f). Transients recorded at wavelengths on the opposite sides of the bleaching maxima featured oscillations with a 180° phase difference (Figure 5g,h).

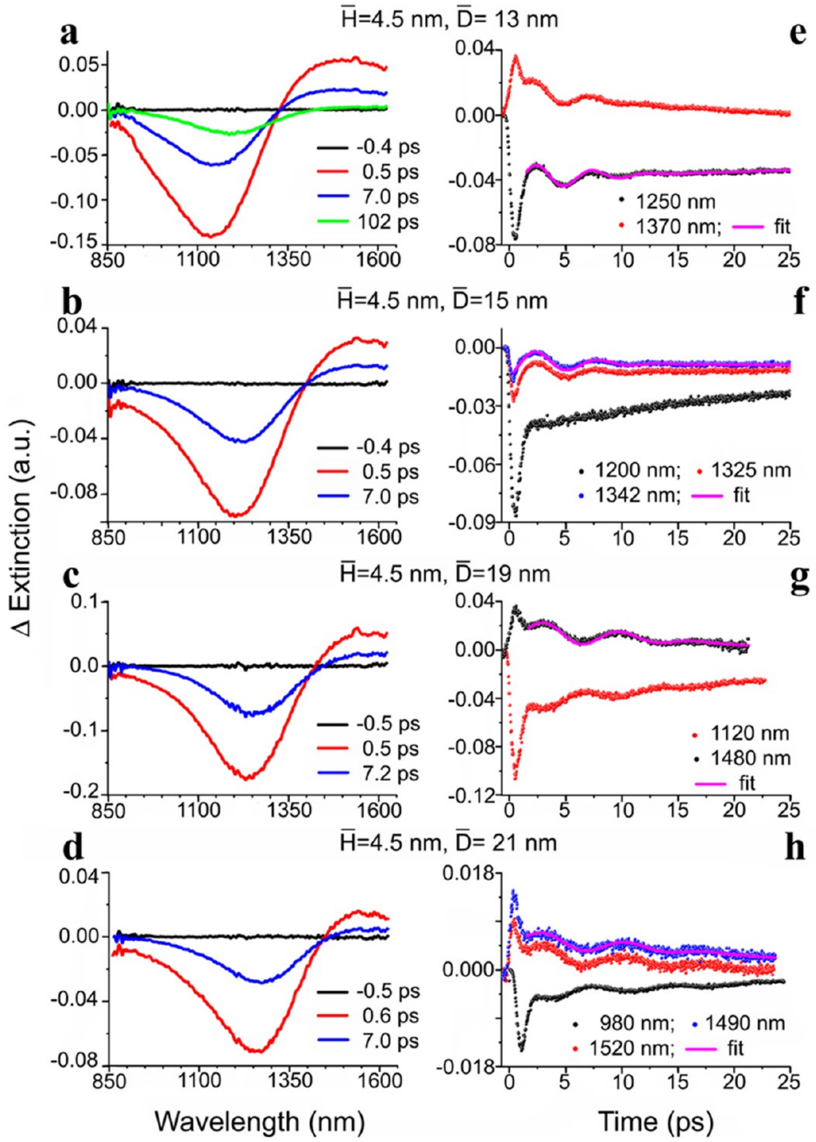

Figure 5. (a−d) TA spectra of variable-size CuS NDs dissolved in toluene, recorded at different delay times. (e, f) Kinetic TA traces of corresponding samples, recorded at selected detection wavelengths (dotted lines), along with the relevant fit curves (solid lines) (see Table 3).

The kinetic TA traces were adequately evaluated using the following function, which describes the oscillatory behavior of the nanocrystal lattice triggered by laser-induced impulsive heating:[76]

$$S(t) = A\left[\cos\left(\frac{2\pi}{T}t+\phi\right)\right]e^{-t^2/\tau^2} \qquad (3)$$

where A is a proportionality constant, $\tau = \bar{D}T/2\sqrt{2\pi}/\eta\sigma_D$ is the damping time, $T = \pi\bar{D}/\eta c_l$ is the measured period of the oscillation, $\bar{D}$ is the mean diameter of the NDs, σ_D is the standard deviation of the Gaussian distribution (with $\sigma_D \ll \bar{D}$), c_l is the longitudinal speed of sound in CuS, and η is an eigenvalue that depends on the traverse and longitudinal speeds of sound. Although eq 3 was derived for spheres, it is applicable to any shape as long as the vibrational motion is confined along a single dimension and the experiments probe all nanocrystals in the ensemble, with the period T of the modulated signal being directly proportional to the mean nanocrystal size.[78] These conditions were fulfilled in the case of the investigated CuS NDs, for which the diameter was indeed much larger than the transverse-axis size ($\bar{D} > \bar{H}$), and, consequently, the induced lattice vibrations should be expected to mostly propagate radially along the longitudinal-axis direction.[79] The satisfactory fitting of the TA data to eq 3 (see magenta solid lines in Figure 5e,f) allowed the observed harmonic modulations of the transients to be unambiguously ascribed to the symmetric radial breathing mode of the NDs activated by pump-pulse-induced lattice heating. Namely, the laser-stimulated vibrational motion of the CuS lattice produced small periodic changes in the ND volume along their major axis, which, in turn, led to a periodic shift of the LSPR spectral position.

Importantly, eq 3 highlights that essential prerequisites to observing pronounced breathing modes are a sufficiently high concentration of free carriers and a narrow size/shape distribution. Actually, the larger the free hole-carrier density, the greater the amount of energy deposited by the ultrafast pump pulse into the free hole gas. Consequently, the higher the lattice temperature reached upon impulsive lattice heating, the more efficient the coherent excitation of the breathing modes. The free hole density is thus accounted for in the amplitude A of the damped cosine function of eq 3. Additionally, it can be considered that, as τ is inversely proportional to the relative standard deviation $\sigma_D/\bar{D}$, harmonic modulations may superimpose to the decay traces only if the condition $\tau > T$ is met. The TA fits allowed estimation of the most relevant parameters underlying the LSPR dynamics, namely, T and τ, as well as σ_D (Table 3). As expected, T scaled up nearly linearly with increasing $\bar{D}$, and $\tau > T$ was verified for all sizes, confirming the TA data interpretation given above. The fact that the kinetic traces revealed up to three accentuated oscillations corroborated the high quality of the ND samples in terms of monodispersity. This was consistent with values of $\sigma_D/\bar{D}$, which ranged between ~7 and ~9%, in accordance with the estimations made directly by TEM (Table 3). To our best knowledge,[2] the detection of the symmetric radial breathing mode for plasmonic–semiconductor nanocrystals by TA spectroscopy techniques is unprecedented.

CONCLUSIONS

This work demonstrates that a vacancy-doped lattice is not a stringent material prerequisite for copper chalcogenide nanocrystals to underlie LSPRs. We have developed a colloidal approach for the phase-selective synthesis of monodisperse copper sulfide NDs, selectively trapped in the stoichiometric, vacancy-free covellite phase, which can indeed support size-dependent LSPRs. The experimental spectra and their geometry dependence have been satisfactorily reproduced and interpreted on the basis of DDA calculations performed within the framework of the Drude–Sommerfeld model. The NDs exhibit a single, intense NIR extinction band that results from the convoluted contributions of a weak out-of-plane and a dominant in-plane dipolar LSPR mode associated with their anisotropic two-dimensional shape. The combined experimental and theoretical analyses of the optical response of the NDs corroborate their inherent metallic-like character with a free hole-carrier density as high as $\sim 10^{22}$ cm^{-3}. The unique electronic properties and the monodispersity of the nanocrystals account for the unprecedented detection of coherent excitation of symmetric radial breathing modes in transient absorption experiments at LSPR wavelengths.

Besides expanding the current library of metal chalcogenide nanostructures and enriching the understanding of LSPR properties in these materials, our study may stimulate progress in all numerous fundamental and practical fields that already greatly benefit from the availability of tailored colloidal nanocrystals of semiconductor and plasmonic materials.

MATERIALS AND METHODS

Synthesis Protocol. Copper(I) chloride (CuCl, 97%), sulfur powder (S, 99.998%), 1-octadecene (ODE, 90%), oleic acid (OLAC, 90%), and oleyl amine (OLAM, 70%) were purchased from Sigma-Aldrich. All solvents used were anhydrous and of analytical grade. Chloroform, tetrachloromethane, and carbon disulfide were purchased from Sigma-Aldrich. Toluene was purchased from Levanchimica. Methanol was purchased from Carlo Erba. Dried acetone (max 0.0075% H_2O) was purchased from SeccoSolv. All chemicals were used as received.

All syntheses were carried out under air-free conditions using a standard Schlenk line setup. Stock reddish S-precursor solution (1 M) in OLAM was prepared in a N_2-protected glovebox by dissolving the required amount of elemental S in degassed OLAM at room temperature.

In a typical preparation, 0.5 mmol of CuCl, 6 mmol of OLAM, 0–40 mmol of OLAC, and 12–50 mmol of ODE were heated in a 50 mL three-neck flask to 130 °C under vacuum for 10 min under vigorous magnetic stirring (note that OLAC alone could not dissolve CuCl). During this period, the solution color gradually turned to light yellow, indicating the formation of stable Cu(I)-based complexes. Then, the mixture was quickly heated to 180 °C under N_2 flow. At this point, 2 mL of the stock S-precursor solution was swiftly added to the flask *via* a disposable syringe. The injection caused the mixture to instantly turn to dark green (which authenticated nanocrystal formation) and the temperature to drop by 30–50 °C, after which it was allowed to recover to 180 °C. The reaction was annealed for 10 min to ensure growth completion.

Nanocrystal evolution was monitored by analyzing aliquots of the hot mixture withdrawn *via* a glass syringe at scheduled time intervals.

After the synthesis, the reaction mixture was allowed to naturally cool to room temperature and transferred to a N_2-protected glovebox. The nanocrystals were induced to flocculate upon addition of an anhydrous methanol/acetone mixture, then separated by centrifugation and purified through repeated cycles of dissolution in $CHCl_3$ and reprecipitation with methanol/acetone. Finally, the nanocrystals were dissolved in the desired nonpolar solvent to yield stable, optically clear colloidal solutions and stored under N_2 atmosphere. No size sorting was performed.

Characterization Techniques. *X-ray Diffraction.* Powder XRD measurements were performed with a D8 Discover-Bruker diffractometer equipped with a Cu source, a Goebel mirror, an Eurelian cradle goniometer, and a scintillator detector. XRD patterns were collected under ambient atmosphere at a fixed incident angle of 3° while moving the detector over the 10–100° range with a step size of 0.05°. Samples were prepared by spreading concentrated solutions of the as-synthesized nanocrystals on a silicon substrate and allowing the solvent to evaporate at room temperature.

The crystal structure of the nanocrystals was first verified by quantitative phase analysis of XRD patterns performed with the whole-profile pattern-fitting program based on the Rietveld method QUANTO.[51] The phase purity of the nanocrystals was checked against the assumption that the samples could include one or more of the following phases: (1) hexagonal covellite (ICSD #63327, space group *P63/mmc*; cell parameters: a = 3.7917 Å; b = 3.7917; c = 16.342 Å; $\alpha = \beta = 90°$; $\gamma = 120°$); (2) hexagonal high-chalcocite Cu_2S (ICSD #166578, space group *P63/mmc*; $a = b$ = 3.89 Å, c = 6.88 Å; $\alpha = \beta = 90°$, $\gamma = 120°$); (3) monoclinic low-chalcocite Cu_2S (ICSD #100333, space group *P*121/*c*1; a = 15.246 Å, b = 11.884 Å, c = 13.494 Å; $\alpha = \gamma = 90°$, $\beta = 116.35°$); (4) cubic digenite $Cu_{1.95}S$ (ICSD #42709, space group $F\bar{4}3m$; cell parameters: $a = b = c$ = 5.564 Å, $\alpha = \beta = \gamma = 90°$); (5) monoclinic djurleite $Cu_{31}S_{16}$ (ICSD # 100334, space group $P12_1/c1$; a = 13.465 Å, b = 15.745 Å, c = 30.058 Å; $\alpha = \gamma = 90.0°$, $\beta = 116.51°$). The weight percentage accuracy of the estimation was better than 5−6%.

The mean coherent crystalline domain size along the different [*h*,*k*,*l*] crystallographic directions, D_{hkl}, was estimated by fitting the XRD patterns of single-phase covellite samples with the whole-profile Rietveld-based program FULLPROF.[53] The following two-step procedure was used. In the first step, the instrumental resolution function (IRF) was evaluated by fitting the XRD pattern of a LaB_6 NIST standard recorded under the same experimental conditions as those used for measuring the samples. The IRF data file was provided separately to the program in order to allow subsequent refinement of the XRD patterns. In the second step, the inhomogeneous line broadening was described by a phenomenological model based on a modified Scherrer formula:

$$\beta_{hkl} = \frac{\lambda}{h\cos\theta} = \frac{\lambda}{\cos\theta}\sum_{\text{imp}} a_{\text{imp}}y_{\text{imp}}(\theta_{\text{h}}, \Phi_{\text{h}}) \qquad (4)$$

where β_{hkl} is the size contribution to the integral width of the (*h*,*k*,*l*) reflection due to an apparent domain size D_{hkl}, and y_{imp} are the real spherical harmonics normalized as described elsewhere.[54] After refinement of the a_{imp} coefficients, the program calculated D_{hkl} along each [*h*,*k*,*l*] direction. Other refinable parameters were the unit-cell parameters. The background was linearly interpolated and unrefined. The quality of the obtained fits was checked by means of a goodness-of-fit statistical indicator (GoF). GoF values of <3−4 were considered to be satisfactory. Note that, due to IRF limitations and strong peak overlapping, meaningful D_{hkl} values could be safely derived only from selected, relatively isolated (*h*,*k*,*l*) reflections with sufficiently high intensity.

Transmission Electron Microscopy. Low-resolution TEM images were recorded with a Jeol JEM 1011 microscope operating at 100 kV. Phase-contrast HRTEM and STEM-ADF experiments were performed using a Jeol JEM 2200 microscope operating at 200 keV, equipped with a Shottky-FEG emitter and an Ω-filter for energy-loss measurements. The objective lens had a spherical aberration coefficient of 0.5 mm. STEM images were acquired with an annular dark-field detector (placed below the filter) at detection angles of 75 to 210 mrad. The as-collected STEM-ADF images were elaborated off-line to deconvolve the effect of the probe by using the software STEM_CELL.[80] The structural parameters used for crystallographic identification were the same as those used for XRD analysis. Samples for TEM measurements were prepared in a N_2-protected glovebox by dropping a dilute toluene solution of freshly prepared nanocrystals onto carbon-coated copper grids and then allowing the solvent to evaporate

Scanning Electron Microscopy. SEM characterization was performed with a FEI NOVAnanoSEM200 microscope. Samples for SEM analysis were prepared in a N_2-protected glovebox by casting a concentrated toluene solution of freshly prepared nanocrystals onto a silicon substrate and then allowing the solvent to evaporate

Elemental Analysis. The Cu and S atomic contents in the nanocrystal powder and solution samples were determined by ICP-AES measurements with a Varian Vista AX spectrometer. The samples for analyses were washed repeatedly and digested in concentrated HCl/HNO_3 (3:1 v/v).

Steady-State Optical Extinction Measurements. Absorption spectra in UV−visible and near-NIR regions were recorded on diluted nanocrystal solutions using a Cary 5 Varian spectrophotometer. The extinction cross sections, $\sigma_{\text{D}}^{\text{exp}}$, at wavelengths corresponding to the plasmon extinction maxima, λ_{LSPR}, were determined as $\sigma_{\text{D}}^{\text{exp}} = \varepsilon(\lambda_{\text{LSPR}})V_{\text{D}}C_{\text{ND}}$, where $\varepsilon(\lambda_{\text{LSPR}})$ is the molar extinction coefficient at λ_{LSPR} (determined by linearly fitting the extinction values to the Lambert−Beer law), V_{ND} is the average nanodisk volume, and C_{ND} is the concentration of the solution expressed as nanodisk moles per liter (determined on the basis of ICP-AES measurements) (Figure S3 in the Supporting Information).

Fourier Transform Infrared Spectroscopy. Infrared spectroscopy measurements in the 4000−400 cm^{-1} spectral range were carried out in transmission mode at a resolution of 4 cm^{-1} using a Bruker Equinox 70 spectrometer. Samples for analysis were prepared by drop-casting nanocrystal solutions onto silicon substrates and allowing the solvent to evaporate. Clean Si wafers were used for baseline correction purposes.

Femtosecond Transient Absorption Spectroscopy Measurements. Samples were prepared in a N_2-protected glovebox by dissolving freshly prepared nanocrystals in toluene. The experiments were conducted with a Clark MXR CPA 2101 laser system in conjunction with an Ultrafast TAPPS HELIOS detection system, consisting primarily of a Er^{3+}-doped glass-fiber-based spectrometer. The output pulses at 387 nm with a 150 fs pulse duration and a 1 kHz repetition rate were used as pump pulses. The samples were transferred to quartz cuvettes with 2 mm optical path under protected atmosphere and pumped at pump fluencies of 120 to 250 $\mu J/cm^2$. TA spectra were recorded in the near-infrared region between 850 and 1650 nm in the magic-angle configuration with respect to the polarization vectors of the pump and probe pulse (the chirp of this spectral range was approximately 350 fs). No photochemical degradation was observed after each experiment, as inferred from the unchanged absorption spectra of the samples recorded after the femtosecond measurements.

TA spectra were obtained as the temporal evolution of the changes in the optical density (ΔOD) of the sample. Therefore, a chopper wheel provided the blocking of each second pump pulse so that the probe pulse was alternately transmitted through a pump-pulse-excited and a ground-state sample. The intensity of the transmitted probe pulse after the pump-pulse-excited sample, $I^*(\lambda,\tau)$, and that without pump-pulse excitation, $I_0(\lambda)$, were measured as a function of the delay time, τ. The ΔOD values were determined as $\Delta\text{OD}(\lambda,\tau) = \log[I_0(\lambda)/I^*(\lambda,\tau)]$.

Theoretical Calculations. Electromagnetic scattering simulations were performed by the discrete dipole approximation method[71,72] using the Amsterdam DDA code.[73] The NDs were modeled as regular hexagonal prisms. The interdipole distance used in all calculations was 0.25 nm. The calculations were carried out using incident polarized plane waves with different polarizations and then performing orientational averaging through a standard tool of the Amsterdam DDA code.[73] To extract ε_∞, ω_{p}, and γ, the experimental extinction cross sections, $\sigma_{\text{D}}^{\text{exp}}(\lambda_i)$, relative to NDs dissolved in CCl_4 were fitted to the computed ones, $\sigma_D^{\text{DDA}}(\lambda_i)$, considering simultaneously four samples of NDs (with $\bar{D}$ = 13, 15, 19, 21 nm and $\bar{H}$ = 5 nm). The following function was minimized:

$$\begin{aligned} \Delta\sigma &= \frac{1}{4}\sum_{D}\Delta\sigma_{\text{D}} \\ \Delta\sigma_{\text{D}} &= \frac{1}{N}\sum_{i=1}^{N}\left|\frac{\sigma_{\text{D}}^{\text{DDA}}(\lambda_i)}{\max[\sigma_{\text{D}}^{\text{DDA}}]} - \frac{\sigma_D^{\text{exp}}(\lambda_i)}{\max[\sigma_{\text{D}}^{\text{exp}}]}\right| \times 100 \end{aligned} \qquad (5)$$

where λ_i ranged from 500 to 2200 nm in steps of 50 nm (thus $N = 35$) and the extinction spectra were taken *normalized* to the corresponding extinction band maxima, $\max[\sigma_{\text{D}}^{\text{DDA}}]$ and $\max[\sigma_{\text{D}}^{\text{exp}}]$ (obtained from a parabolic fit), to avoid inaccuracies in the absolute intensity of the scattering cross sections. The approach of fitting several spectra at once allowed reducing the statistical error.

The experimental data were fitted through a three-dimensional scan of the relevant parameters, as follows: ω_{p} was varied from 3.4 to 5.1 eV in steps of 0.1 eV; ε_∞ was varied from 1 to 11 in steps of 2; γ was varied from 0.2 to 0.6 eV in steps of 0.05 eV. The discretization of the three-dimensional space led to a sampling error on $\Delta\sigma$ on the order of 2%. Globally, $18 \times 5 \times 8 \times 4 \times 35 = 100800$ DDA calculations including orientational averaging were performed.

Conflict of Interest: The authors declare no competing financial interest.

Supporting Information Available: FT-IR spectra of nanocrystals synthesized in different surfactant mixtures at 180 °C; TEM, XRD, and ICP-AES data on nanocrystals synthesized at higher temperatures; calculation of extinction cross sections; effect of ε_∞ and of ω_p on the DDA-computed extinction cross sections. This material is available free of charge *via* the Internet at http://pubs.acs.org.

Acknowledgment. This work was supported by the Italian Ministry of Education, University and Research through project AEROCOMP (Contract MIUR No. DM48391). Partial financial support from the Fondazione Cariplo through Project No. 2010-0612 "Chemical synthesis and characterization of magneto-plasmonic nano-heterostructures" and from the European Research Council (ERC) through Starting Grant FP7 Project DEDOM (grant agreement no. 207441) is also gratefully acknowledged.

REFERENCES AND NOTES

1. Routzahn, A. L.; White, S. L.; Fong, L.-K.; Jain, P. K. Plasmonics with Doped Quantum Dots. *Isr. J. Chem.* **2012**, *52*, 983–991.
2. Scotognella, F.; Valle, G.; Srimath Kandada, A.; Zavelani-Rossi, M.; Longhi, S.; Lanzani, G.; Tassone, F. Plasmonics in Heavily-Doped Semiconductor Nanocrystals. *Eur. Phys. J. D* **2013**, *86*, 1–13.
3. Zhao, Y. X.; Pan, H. C.; Lou, Y. B.; Qiu, X. F.; Zhu, J. J.; Burda, C. Plasmonic Cu$_{2-x}$S Nanocrystals: Optical and Structural Properties of Copper-Deficient Copper(I) Sulfides. *J. Am. Chem. Soc.* **2009**, *131*, 4253–4261.
4. Wang, Y.; Hu, Y.; Zhang, Q.; Ge, J.; Lu, Z.; Hou, Y.; Yin, Y. One-Pot Synthesis and Optical Property of Copper(I) Sulfide Nanodisks. *Inorg. Chem.* **2010**, *49*, 6601–6608.
5. Luther, J. M.; Jain, P. K.; Ewers, T.; Alivisatos, A. P. Localized Surface Plasmon Resonances Arising from Free Carriers in Doped Quantum Dots. *Nat. Mater.* **2011**, *10*, 361–366.
6. Hsu, S.-W.; On, K.; Tao, A. R. Localized Surface Plasmon Resonances of Anisotropic Semiconductor Nanocrystals. *J. Am. Chem. Soc.* **2011**, *133*, 19072–19075.
7. Kruszynska, M.; Borchert, H.; Bachmatiuk, A.; Rümmeli, M. H.; Büchner, B.; Parisi, J.; Kolny-Olesiak, J. Size and Shape Control of Colloidal Copper(I) Sulfide Nanorods. *ACS Nano* **2012**, *6*, 5889–5896.
8. Liu, X.; Wang, X.; Zhou, B.; Law, W.-C.; Cartwright, A. N.; Swihart, M. T. Size-Controlled Synthesis of Cu$_{2-x}$E (E = S, Se) Nanocrystals with Strong Tunable Near-Infrared Localized Surface Plasmon Resonance and High Conductivity in Thin Films. *Adv. Funct. Mater.* **2012**, *23*, 1256–1264.
9. Dorfs, D.; Hartling, T.; Miszta, K.; Bigall, N. C.; Kim, M. R.; Genovese, A.; Falqui, A.; Povia, M.; Manna, L. Reversible Tunability of the Near-Infrared Valence Band Plasmon Resonance in Cu$_{2-x}$Se Nanocrystals. *J. Am. Chem. Soc.* **2011**, *133*, 11175–11180.
10. Dilena, E.; Dorfs, D.; George, C.; Miszta, K.; Povia, M.; Genovese, A.; Casu, A.; Prato, M.; Manna, L. Colloidal Cu$_{2-x}$(S$_y$Se$_{1-y}$) Alloy Nanocrystals with Controllable Crystal Phase: Synthesis, Plasmonic Properties, Cation Exchange and Electrochemical Lithiation. *J. Mater. Chem.* **2012**, *22*, 13023–13031.
11. Kriegel, I.; Rodríguez-Fernández, J.; Wisnet, A.; Zhang, H.; Waurisch, C.; Eychmuller, A.; Dubavik, A.; Govorov, A. O.; Feldmann, J. Shedding Light on Vacancy-Doped Copper Chalcogenides: Shape-Controlled Synthesis, Optical Properties, and Modeling of Copper Telluride Nanocrystals with Near-Infrared Plasmon Resonances. *ACS Nano* **2013**, *7*, 4367–4377.
12. Kriegel, I.; Jiang, C.; Rodriguez-Fernandez, J.; Schaller, R. D.; Talapin, D. V.; Da Como, E.; Feldmann, J. Tuning the Excitonic and Plasmonic Properties of Copper Chalcogenide Nanocrystals. *J. Am. Chem. Soc.* **2012**, *134*, 1583–1590.
13. Hsu, S.-W.; Bryks, W.; Tao, A. R. Effects of Carrier Density and Shape on the Localized Surface Plasmon Resonances of Cu$_{2-x}$S Nanodisks. *Chem. Mater.* **2012**, *24*, 3765–3771.
14. Zhao, Y. X.; Burda, C. Development of Plasmonic Semiconductor Nanomaterials with Copper Chalcogenides for a Future with Sustainable Energy Materials. *Energy Environ. Sci.* **2012**, *5*, 5564–5576.
15. Scotognella, F.; Della Valle, G.; Srimath Kandada, A. R.; Dorfs, D.; Zavelani-Rossi, M.; Conforti, M.; Miszta, K.; Comin, A.; Korobchevskaya, K.; Lanzani, G.; Manna, L.; Tassone, F. Plasmon Dynamics in Colloidal Cu$_{2-x}$Se Nanocrystals. *Nano Lett.* **2011**, *11*, 4711–4717.
16. Mendelsberg, R. J.; Garcia, G.; Li, H.; Manna, L.; Milliron, D. J. Understanding the Plasmon Resonance in Ensembles of Degenerately Doped Semiconductor Nanocrystals. *J. Phys. Chem. C* **2012**, *116*, 12226–12231.
17. Du, W.; Qian, X.; Ma, X.; Gong, Q.; Cao, H.; Yin, J. Shape-Controlled Synthesis and Self-Assembly of Hexagonal Covellite (CuS) Nanoplatelets. *Chem.—Eur. J.* **2007**, *13*, 3241–3247.
18. Zhang, H.; Zhang, Y.; Yu, J.; Yang, D. Phase-Selective Synthesis and Self-Assembly of Monodisperse Copper Sulfide Nanocrystals. *J. Phys. Chem. C* **2008**, *112*, 13390–13394.
19. Lim, W. P.; Wong, C. T.; Ang, S. L.; Low, H. Y.; Chin, W. S. Phase-Selective Synthesis of Copper Sulfide Nanocrystals. *Chem. Mater.* **2006**, *18*, 6170–6177.
20. Larsen, T. H.; Sigman, M.; Ghezelbash, A.; Doty, R. C.; Korgel, B. A. Solventless Synthesis of Copper Sulfide Nanorods by Thermolysis of a Single Source Thiolate-Derived Precursor. *J. Am. Chem. Soc.* **2003**, *125*, 5638–5639.
21. Yi, L.; Gao, M. From Ultrathin Two-Dimensional Djurleite Nanosheets to One-Dimensional Nanorods Comprised of Djurleite Nanoplates: Synthesis, Characterization, and Formation Mechanism. *Cryst. Growth Des.* **2011**, *11*, 1109–1116.
22. Abdelhady, A. L.; Ramasamy, K.; Malik, M. A.; O'Brien, P.; Haigh, S. J.; Raftery, J. New Routes to Copper Sulfide Nanostructures and Thin Films. *J. Mater. Chem.* **2011**, *21*, 17888–17895.
23. Ghezelbash, A.; Korgel, B. A. Nickel Sulfide and Copper Sulfide Nanocrystal Synthesis and Polymorphism. *Langmuir* **2005**, *21*, 9451–9456.
24. Mott, D.; Yin, J.; Engelhard, M.; Loukrakpam, R.; Chang, P.; Miller, G.; Bae, I.-T.; Chandra Das, N.; Wang, C.; Luo, J.; *et al.* From Ultrafine Thiolate-Capped Copper Nanoclusters toward Copper Sulfide Nanodiscs: A Thermally Activated Evolution Route. *Chem. Mater.* **2010**, *22*, 261–271.
25. Lou, W.; Chen, M.; Wang, X.; Liu, W. Size Control of Monodisperse Copper Sulfide Faceted Nanocrystals and Triangular Nanoplates. *J. Phys. Chem. C* **2007**, *111*, 9658–9663.
26. Grijalva, H.; Inoue, M.; Boggavarapu, S.; Calvert, P. Amorphous and Crystalline Copper Sulfides, CuS. *J. Mater. Chem.* **1996**, *6*, 1157–1160.
27. Nozaki, H.; Shibata, K.; Ohhashi, N. Metallic Hole Conduction in CuS. *J. Solid State Chem.* **1991**, *91*, 306–311.
28. Liang, W.; Whangbo, M. H. Conductivity Anisotropy and Structural Phase Transition in Covellite CuS. *Solid State Commun.* **1993**, *85*, 405–408.
29. Adelifard, M.; Eshghi, H.; Mohagheghi, M. M. B. An Investigation on Substrate Temperature and Copper to Sulphur Molar Ratios on Optical and Electrical Properties of Nanostructural CuS Thin Films Prepared by Spray Pyrolysis Method. *Appl. Surf. Sci.* **2012**, *258*, 5733–5738.
30. Rodríguez-Lazcano, Y.; Martínez, H.; Calixto-Rodríguez, M.; Núñez Rodríguez, A. Properties of CuS Thin Films Treated in Air Plasma. *Thin Solid Films* **2009**, *517*, 5951–5955.
31. Mazin, I. Structural and Electronic Properties of the Two-Dimensional Superconductor CuS with 1 1/3-Valent Copper. *Phys. Rev. B* **2012**, 85.
32. Yuan, K. D.; Wu, J. J.; Liu, M. L.; Zhang, L. L.; Xu, F. F.; Chen, L. D.; Huang, F. Q. Fabrication and Microstructure of p-Type Transparent Conducting CuS Thin Film and Its Application in Dye-Sensitized Solar Cell. *Appl. Phys. Lett.* **2008**, *93*, 132106.
33. Gainov, R. R.; Dooglav, A. V.; Pen'kov, I. N.; Mukhamedshin, I. R.; Mozgova, N. N.; Evlampiev, I. A.; Bryzgalov, I. A. Phase

Transition and Anomalous Electronic Behavior in the Layered Superconductor CuS Probed by NQR. *Phys. Rev. B* **2009**, 79.
34. Pearce, C. I.; Pattrick, R. A. D.; Vaughan, D. J. Electrical and Magnetic Properties of Sulfides. *Sulfide Miner. Geochem.* **2006**, *61*, 127–180.
35. Pearce, C. I.; Pattrick, R. A. D.; Vaughan, D. J.; Henderson, C. M. B.; van der Laan, G. Copper Oxidation State in Chalcopyrite: Mixed Cu d(9) and d(10) Characteristics. *Geochim. Cosmochim. Acta* **2006**, *70*, 4635–4642.
36. Saito, S.; Kishi, H.; Nie, K.; Nakamaru, H.; Wagatsuma, F.; Shinohara, T. Cu-63 NMR Studies of Copper Sulfide. *Phys. Rev. B* **1997**, *55*, 14527–14535.
37. Goh, S. W.; Buckley, A. N.; Lamb, R. N.; Rosenberg, R. A.; Moran, D. The Oxidation States of Copper and Iron in Mineral Sulfides, and the Oxides Formed on Initial Exposure of Chalcopyrite and Bornite to Air. *Geochim. Cosmochim. Acta* **2006**, *70*, 2210–2228.
38. Kumar, P.; Nagarajan, R. Sarangi, R. Quantitative X-ray Absorption and Emission Spectroscopies: Electronic Structure Elucidation of Cu_2S and CuS. *J. Mater. Chem. C* **2013**, *1*, 2448–2454.
39. On the basis of earlier magnetic studies, X-ray diffraction, X-ray absorption, and X-ray photoelectron spectroscopy investigations [refs 26, 27, 34, 35], covellite CuS was described as an entirely monovalent Cu(+1) sulfide compound containing mixed monosulfide and disulfide anions, through the formula $(Cu^+)_3(S)^{2-}(S_2)^-$, where a S 3p hole is associated with a disulfide unit $(S_2)^{2-}$. In the proposed model supported by calculations [refs 26, 27], CuS accommodates holes delocalized with S 3p orbitals of the valence band. More recently, the electronic properties of CuS have been revisited by nuclear magnetic resonance [refs 33, 36] and quantitative X-ray absorption and emission spectroscopy measurements [ref 38]. CuS has been reinterpreted as a mixed Cu(+1)/Cu(+2) sulfide with the formula $[(Cu_2)]^{3+}(Cu)^+(S)^{2-}(S_2)^{2-}$, where the valence of copper ions is intermediate between monovalent and divalent states (depending on the lattice coordination environment), and Cu^{2+}-based 3d holes delocalize in the S 3p valence band. First-principles calculations have independently supported the latter picture [ref 31].
40. Konev, V. N.; Chebotin, V. N.; Fomenkov, S. A. Diffusion Phenomena in Nonstoichiometric Copper Sulfide and Selenide. *Inorg. Mater.* **1985**, *21*, 166–170.
41. Konev, V. N.; Fomenkov, S. A.; Chebotin, V. N. Thermodiffusion of Copper Atoms in Nonstoichiometric Copper Sulfide and Selenide. *Inorg. Mater.* **1985**, *21*, 163–165.
42. Cassaignon, S.; Sanchez, S.; Guillemoles, J.-F.; Vedela, J.; Gomez Meier, H. Influence of the Composition on the Copper Diffusion in Copper Sulfides Study by Impedance Spectroscopy. *J. Electrochem. Soc.* **1999**, *146*, 4666–4671.
43. Cassaignon, S.; Pauporté, T.; Guillemoles, J.-F.; Vedel, J. Copper Diffusion in Copper Sulfide: A Systematic Study. *Ionics* **1998**, *4*, 364–371.
44. Dunn, J. G.; Muzenda, C. Quantitative Analysis of Phases Formed during the Oxidation of Covellite (CuS). *J. Therm. Anal. Calorim.* **2001**, *64*, 1241–1246.
45. Dunn, J. G.; Muzenda, C. Thermal Oxidation of Covellite (CuS). *Thermochim. Acta* **2001**, *369*, 117–123.
46. Waldner, P.; Sitte, W. Digenite $Cu_{2-x}S$: Thermodynamic Analysis of Sulfur Activities. *Monatsh. Chem.* **2012**, *143*, 1215–1218.
47. Chakrabarti, D. J., Laughlin, D. E. In *Phase Diagrams of Binary Copper Alloys*; Subramanian, P. R., Ed.; ASM International: Materials Park, 1994.
48. Wu, H.; Chen, W. Synthesis and Reaction Temperature-Tailored Self-Assembly of Copper Sulfide Nanoplates. *Nanoscale* **2011**, *3*, 5096–5102.
49. Pagès, C.; Coppel, Y.; Kahn, M. L.; Maisonnat, A.; Chaudret, B. Self-Assembly of ZnO Nanocrystals in Colloidal Solutions. *Chem. Phys. Chem.* **2009**, *10*, 2334–2344.
50. Coppel, Y.; Spataro, G.; Collière, V.; Chaudret, B.; Mingotaud, C.; Maisonnat, A.; Kahn, M. L. Self-Assembly of ZnO Nanoparticles – An NMR Spectroscopic Study. *Eur. J. Inorg. Chem.* **2012**, 2691–2699.
51. Altomare, A.; Burla, M. C.; Giacovazzo, C.; Guagliardi, A.; Moliterni, A. G. G.; Polidori, G.; Rizzi, R. Quanto: A Rietveld Program for Quantitative Phase Analysis of Polycrystalline Mixtures. *J. Appl. Crystallogr.* **2001**, *34*, 392–397.
52. Mu, C.-F.; Yao, Q.-Z.; Qu, X.-F.; Zhou, G.-T.; Li, M.-L.; Fu, S.-Q. Controlled Synthesis of Various Hierarchical Nanostructures of Copper Sulfide by a Facile Microwave Irradiation Method. *Colloids Surf. A* **2010**, *371*, 14–21.
53. Crystallographic Tools for Rietveld, Profile Matching and Integrated Intensity Refinements of X-ray and/or Neutron Data, available online at http://wwwold.ill.fr/dif/Soft/fp/php/downloads.html.
54. Järvinen, M. Application of Symmetrized Harmonics Expansion to Correction of the Preferred Orientation Effect. *J. Appl. Crystallogr.* **1993**, *26*, 525–531.
55. Joo, J.; Na, H. B.; Yu, T.; Yu, J. H.; Kim, Y. W.; Wu, F.; Zhang, J. Z.; Hyeon, T. Generalized and Facile Synthesis of Semiconducting Metal Sulfide Nanocrystals. *J. Am. Chem. Soc.* **2003**, *125*, 11100–11105.
56. Seo, J.-w.; Jun, Y.-w.; Ko, S. J.; Cheon, J. *In Situ* One-Pot Synthesis of 1-Dimensional Transition Metal Oxide Nanocrystals. *J. Phys. Chem. B* **2005**, *109*, 5389–5391.
57. Ye, E.; Zhang, S.-Y.; Liu, S.; Han, M.-Y. Disproportionation for Growing Copper Nanowires and Their Controlled Self-Assembly Facilitated by Ligand Exchange. *Chem.—Eur. J.* **2011**, *17*, 3074–3077.
58. Baum, T. H.; Larson, C. E.; May, G. Ligand-Stabilized Copper-(I) Hexafluoroacetylacetonate Complexes - NMR Spectroscopy and the Nature of the Copper-Alkene Bond. *J. Organomet. Chem.* **1992**, *425*, 189–200.
59. Bellott, B. J.; Girolami, G. S. Structures and Properties of Copper Alkene Complexes. Preorganization Effects and the Binding of Different Isomers of Cyclododecatriene to Copper Triflate. *Organometallics* **2009**, *28*, 2046–2052.
60. Krisyuk, V. V.; Turgambaeva, A. E.; Rhee, S. W. Homobinuclear Copper(I) Hexafluoroacetylacetonate Complexes with Non-Cyclic Diene Ligands. *Polyhedron* **2004**, *23*, 809–813.
61. Goles, S. J.; Faulds, P.; Hursthouse, M. B.; Kelly, D. G.; Toner, A. J. Synthesis and Reactivity of Copper(I) Phosphine-Alkene Complexes: X-ray Crystal Structure of $CuCl(Ph_2PCPh{=}CH_2)_2$. *Polyhedron* **2000**, *19*, 1271–1278.
62. *Advanced Wet-Chemical Synthetic Approaches to Inorganic Nanostructures*; Cozzoli, P.D., Ed.; Transworld Research Network: Kerala (India), 2008.
63. Yin, M.; Wu, C.-K.; Lou, Y.; Burda, C.; Koberstein, J. T.; Zhu, Y.; O'Brien, S. Copper Oxide Nanocrystals. *J. Am. Chem. Soc.* **2005**, *127*, 9506–9511.
64. Thomson, J. W.; Nagashima, K.; Macdonald, P. M.; Ozin, G. A. From Sulfur–Amine Solutions to Metal Sulfide Nanocrystals: Peering into the Oleylamine–Sulfur Black Box. *J. Am. Chem. Soc.* **2011**, *133*, 5036–5041.
65. Li, Z.; Ji, Y.; Xie, R.; Grisham, S. Y.; Peng, X. Correlation of CdS Nanocrystal Formation with Elemental Sulfur Activation and Its Implication in Synthetic Development. *J. Am. Chem. Soc.* **2011**, *133*, 17248–17256.
66. Lukashev, P.; Lambrecht, W. R. L.; Kotani, T.; van Schilfgaarde, M. Electronic and Crystal Structure of $Cu_{2-x}S$: Full-Potential Electronic Structure Calculations. *Phys. Rev. B* **2007**, 76.
67. Sönnichsen, C.; Franzl, T.; Wilk, T.; von Plessen, G.; Feldmann, J.; Wilson, O.; Mulvaney, P. Drastic Reduction of Plasmon Damping in Gold Nanorods. *Phys. Rev. Lett.* **2002**, *88*, 077402.
68. Maillard, M.; Giorgio, S.; Pileni, M.-P. Tuning the Size of Silver Nanodisks with Similar Aspect Ratios: Synthesis and Optical Properties. *J. Phys. Chem. B* **2003**, *107*, 2466–2470.
69. Kelly, K. L.; Coronado, E.; Zhao, L. L.; Schatz, G. C. The Optical Properties of Metal Nanoparticles: The Influence of Size, Shape, and Dielectric Environment. *J. Phys. Chem. B* **2003**, *107*, 668–677.
70. Brioude, A.; Pileni, M. P. Silver Nanodisks: Optical Properties Study Using the Discrete Dipole Approximation Method. *J. Phys. Chem. B* **2005**, *109*, 23371–23377.

71. Draine, B. T.; Flatau, P. J. Discrete-Dipole Approximation for Scattering Calculations. *J. Opt. Soc. Am. A* **1994**, *11*, 1491–1499.
72. Yurkin, M. A.; Hoekstra, A. G. The Discrete Dipole Approximation: An Overview and Recent Developments. *J. Quant. Spectrosc. Radiat. Transfer* **2007**, *106*, 558–589.
73. http://code.google.com/p/a-dda/
74. Coronado, E. A.; Schatz, G. C. Surface Plasmon Broadening for Arbitrary Shape Nanoparticles: A Geometrical Probability Approach. *J. Chem. Phys.* **2003**, *119*, 3926–3934.
75. Hartland, G. V. Optical Studies of Dynamics in Noble Metal Nanostructures. *Chem. Rev.* **2011**, *111*, 3858–3887.
76. Hartland, G. V. Coherent Vibrational Motion in Metal Particles: Determination of the Vibrational Amplitude and Excitation Mechanism. *J. Chem. Phys.* **2002**, *116*, 8048–8055.
77. Voisin, C.; Del Fatti, N.; Christofilos, D.; Vallée, F. Ultrafast Electron Dynamics and Optical Nonlinearities in Metal Nanoparticles. *J. Phys. Chem. B* **2001**, *105*, 2264–2280.
78. Wang, L.; Nishijima, Y.; Ueno, K.; Misawa, H.; Tamai, N. Near-IR Vibrational Dynamics of Periodic Gold Single and Pair Nanocuboids. *Appl. Phys. Lett.* **2009**, *95*, 053116.
79. Langhammer, C.; Yuan, Z.; Zorić, I.; Kasemo, B. Plasmonic Properties of Supported Pt and Pd Nanostructures. *Nano Lett.* **2006**, *6*, 833–838.
80. Grillo, V. Advances in STEM-CELL. A Free Software for TEM and STEM Analysis and Simulations: Probe Deconvolution in STEM-HAADF. *Microsc. Microanal.* **2011**, *17*, 1292–1293.